J. Fluid Mech. (2024), *vol*. 985, A22, doi:10.1017/jfm.2024.308

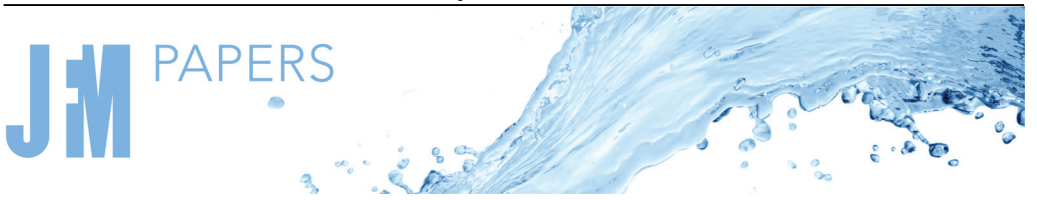

Turbulence over young wind waves dominated by capillaries and micro-breakers

Jitae Do[1], **Binbin Wang**[2] **and Kuang-An Chang**[1,3],†

[1]Department of Ocean Engineering, Texas A&M University, College Station, TX 77843, USA

[2]Department of Civil & Environmental Engineering, University of Missouri, Columbia, MO 65211, USA

[3]Zachry Department of Civil & Environmental Engineering, Texas A&M University, College Station, TX 77843, USA

(Received 14 August 2023; revised 6 December 2023; accepted 18 March 2024)

We conducted experiments in a laboratory to study turbulent flow over wind generated water waves. The experiments were performed in a wind-wave-current flume with three free stream wind speeds of $U_{ref} = 6.0$, 8.0 and 10.0 m s^{-1}, corresponding to 10 m equivalent wind speed of $U_{10} = 10.2$, 12.2 and 14.1 m s^{-1} and the root-mean-square wave height of 0.7, 1.1 and 1.7 cm, respectively, at a fetch of 6.2 m. The instantaneous velocity fields above the waves were obtained by using a particle image velocimetry (PIV) technique. The velocity fields were decomposed into the mean, wave-induced and turbulent velocity components. The tested wind waves were primarily dissipated by capillaries and microscale breaking waves. The Bond number and the shear velocity-fetch based Reynolds number were found to correlate with the wind wave regimes well. The turbulent dissipation rates above the water surface were determined based on resolved spatial gradient of instantaneous velocities, where the time-averaged dissipation rate values were calibrated using those estimated from the one-dimensional velocity spectrum in the temporal space. Subsequently, the turbulent kinetic energy (TKE) budget including its production, dissipation, advection and turbulent transport was presented. In addition, conditional averaging analysis of the TKE budgets over leeward, windward sides and all phases was performed. The results showed a strong dependency with the wave phase in the TKE budget terms except for the dissipation. The production-dissipation ratio increased significantly as the wind speed increased, likely attributed to the increased roughness over the substantial coverage of micro-breaking waves.

Key words: wind–wave interactions, surface gravity waves

† Email address for correspondence: kchang@tamu.edu

1. Introduction

When wind blows over the water surface, the waves are generated by the wind. These surface waves are shaped by wind drag, evolve dynamically in both time and space, interact with the overlying wind, and affect the turbulence in both air and water. Although the process of wave generation and growth has received attention (Miles 1957; Phillips 1957; Blennerhassett & Stuart 1997), a complete description of the phenomenon is not sufficiently revealed. The difficulty roots from its interconnected characteristics with the turbulent flows in both air and water in the process of wave generation and growth, and the nonlinearity of wind waves in space and time (Pizzo, Deike & Ayet 2021).

To understand the turbulence over wind-wave fields, numerical studies including direct numerical simulation (DNS) and large eddy simulation (LES) have been very useful in providing statistics and mechanisms of turbulent flow above various waves or wavy boundaries (Sullivan, McWilliams & Moeng 2000; Shen *et al*. 2003; Rutgersson & Sullivan 2005; Yang & Shen 2010; Husain *et al*. 2019). For instance, the time-averaged vertical profiles of turbulent intensities above the wavy surface and the spatial distribution of Reynolds shear stress over various phases of waves show a dependence on the wave age defined as c_p/u_*, where c_p is the wave speed and u_* is shear velocity or friction velocity (Sullivan *et al*. 2000; Rutgersson & Sullivan 2005; Yang & Shen 2010). The comparisons among different wave fields (e.g. Airy waves versus Stokes waves) allowed for evaluating the effect of wave nonlinearity on the pressure distribution and hence its effect on the wave growth rate (Shen *et al*. 2003; Yang & Shen 2010). More recently, it was found that the nonlinear stage of wave growth is dependent on wavelength with fully coupled wind-wave simulations (Wu & Deike 2021). The resolvable turbulent statistics in small scales by numerical models enables the budget analysis for turbulent kinetic energy (TKE) and for the kinetic energy of the wave-induced velocity field (Rutgersson & Sullivan 2005; Yang & Shen 2010). Although the numerical simulations provide valuable information about details of turbulence above various wave fields, these simulated waves are oversimplified and hence do not represent the full physics of wind waves (e.g. the effect of wave morphology on the overlying wind turbulence).

However, laboratory and field experiments offer observational data of wave and flow fields, which grant direct interpretation of the underlying physics and can also be used for model validations. In the early years, intrusive probes such as hot wire and Pitot tube were widely used to measure airflow above wind-generated surface waves (Toba 1961; Stewart 1970; Wu 1975; Hsu, Hsu & Street 1981, Hsu et al. 1982; Hsu & Hsu 1983). In last few decades, non-intrusive techniques such as particle image velocimetry (PIV) have been widely used for flow and turbulence measurements in laboratory environments (Keane & Adrian 1992; Raffel, Willert & Kompenhans 1998). PIV has also been deployed in the field to study water turbulence immediately below the air–water interface (Wang *et al.* 2015; Wang & Liao 2016). However, the application of PIV in studying airflow above wind waves has been limited due to challenges in particle seeding, and arrangement of laser and camera in wind-wave tanks with moving and deformable surface waves. The application in such environments was initially introduced by Reul, Branger & Giovanangeli (1999) to visualize the airflow separation close to the sharp crest over wind generated breaking waves. Shaikh & Siddiqui (2010) investigated the vertical profiles of mean velocity, turbulent intensities, Reynolds shear stress, and production and dissipation rate of TKE above wind waves at a 2 m fetch with wind speeds of 1.5–4.4 m s^{-1} against a reference of wavy solid surface and a smooth wall. They found that, under the same wind speed, the mean flow above the wavy water surface has the smallest friction velocity among the smooth wall, solid wavy surface and wind-wave surface. Therefore, the effect of moving water waves on the

surface drag must be considered while using theoretically calculated friction velocity in scaling turbulent parameters.

Using PIV for flow measurements in wind-wave fields can effectively reveal the wave-coherent turbulent characteristics at different stages of wind waves. For instance, Buckley & Veron (2016) observed intensified Reynolds shear stress on the leeward side of young waves ($c_p/u_* = 3.7$) and more uniform distribution for older waves ($c_p/u_* = 6.5$). The Reynolds shear stress is significantly suppressed within the critical boundary layer where wave speed lags airflow. Under combined wind and mechanically induced waves at swell conditions ($c_p/u_* = 31.7$), heightened Reynolds shear stress emerges within the critical layer and windward side, contrasting the wind-wave behaviour. Further analysis by Buckley & Veron (2019) dissected TKE production, emphasizing significant TKE production linked to Reynolds normal stress in the horizontal direction and the horizontal velocity gradients for young waves ($c_p/u_* = 1.4$). Using triple-decomposition, Yousefi, Veron & Buckley (2021) examined the TKE production and the production of kinetic energy associated with wave-induced velocity field. Their analysis on the wave–turbulence interaction term indicated the mechanism of energy transfer from wave-induced flow to the turbulence field, particularly for young waves.

What has been missing in the literature is the accurate measurement of TKE dissipation rate. Depending on the wind speed, the Kolmogorov length scale of the airflow above the wind waves are typically in the range of O(10–100 μm). This requires a comparable spatial resolution in the PIV-resolved flow field to accurately estimate the gradient velocity of fluctuations for directly calculating turbulent dissipation rate (Doron *et al*. 2001; Luznik *et al*. 2007). The needed spatial resolution is typically smaller than what PIV can offer while maintaining a field of view (FOV) large enough to resolve different wave phases. Therefore, the turbulent dissipation rate is often estimated as a part of the residual term in TKE budget analysis (Yousefi *et al*. 2021). This approach presents challenges in a complete analysis of TKE budget, as the residual includes measurement uncertainty and other non-resolvable terms such as pressure transport.

To address this data gap, here we present a time-resolved PIV measurement with a sampling rate of 2400 Hz over wind-wave fields at three different wind speeds (6.0, 8.0 and 10.0 m s^{-1}). The time series velocity data with the high temporal resolution allows for resolving the inertial subrange, which exhibits a universal −5/3 Kolmogorov law in the energy spectrum for fully developed turbulence and can be used to estimate turbulent dissipation rate (Kolmogorov 1941; Tennekes & Lumley 1972). Because the inertial subrange is much larger than the Kolmogorov length scale, the requirement for the turbulence sampling rate is much more relaxed. For instance, the universal Kolmogorov scaling was observed with measurements of wind speed at the sampling rate of O(10–100 Hz) in the airflow over the ocean based on the field measurements made in the offshore of Southern California from the floating instrument platform (FLIP) (Ortiz-Suslow & Wang 2019; Ortiz-Suslow *et al*. 2020). Although this is not a requirement, we note that the sampling time interval (∼0.42 ms) is smaller than the estimated Kolmogorov time scale (1.8–3.9 ms) in the current study. The TKE dissipation rate estimated from the energy spectrum can be further used as a benchmark to correct the value estimated through the direct calculation of velocity gradient tensor (Wu *et al*. 2021). Using this approach, our objective is to quantify the spatial distribution of TKE dissipation rate immediately above the air–water interface, and hence yield insights into the small-scale processes within the wind-wave field. From a numerical perspective, Husain *et al*. (2019) found that the turbulent dissipation rate is most pronounced at the trailing edge of wave crest and is subsequently advected downstream in their numerical

simulations. Our measurements will provide observational data to investigate these phase-coherent features. Furthermore, the measured turbulent dissipation rate will allow for more accurate TKE budget analysis, which is currently missing in the literature.

The present experimental work is designed for young, growing waves without air-entraining breakers. In the wind-wave field, the surface waves can be classified into different regimes depending on the dominant wavelength and the surface morphology of the waves due to molecular viscosity, generation of capillary waves, and micro- and macro-breaking waves (Caulliez 2013). Among these regimes, microscale breaking is a common feature that contributes significantly to the heat and gas transfer across the air–water interface (Jessup, Zappa & Yeh 1997; Zappa *et al*. 2004). Micro-breaking waves are featured by the formation of a bulge on the forward face of the wave crest following a train of capillary ripples (Banner & Phillips 1974; Duncan *et al*. 1999). Using the vorticity field measured in the water side, Loewen & Siddiqui (2006) and Siddiqui & Loewen (2007) quantified that the percentage of microscale breaking increased significantly from 11 % to 80 % with increasing wind speed from 4.5 to 7.4 m s^{-1} and reached 90 % with wind speed of 11.0 m s^{-1} at a fetch of 5.5 m in a wind-wave tank.

While the micro-breakings are commonly present in wind-waves generated in a laboratory, no experimental study has focused on the effect of micro-breaking waves on the overlying turbulence structures, particularly on the small-scale process, e.g. dissipation rate of TKE. The existing experimental work (Buckley & Veron 2016, 2019; Yousefi & Veron 2020, Yousefi *et al*. 2021) likely covered micro- and macro-breaking wave regimes, but the focus has been on the TKE production, wave–turbulence interactions and kinetic energy budget analysis without measurement of turbulent dissipation rate. In addition, the transition between wave regimes and associated wave-morphological changes are very sensitive to the wind speed (Siddiqui & Loewen 2007); how turbulence responds to the change of wave surface is not characterized. In this study, we test three wind speeds to represent the microscale breaking regime: one positioned near the transition point from the capillary wave regime, the second located in the middle of the microscale breaking wave regime and the third near the threshold where macroscale breaking is imminent. As such, our study provides unique experimental conditions to evaluate whether different stages of wind waves in the microscale breaking regime would affect the overlying turbulence with very similar wave ages ($c_p/u_* = 1.03$–1.10).

This paper is organized as follows. Section 2 describes the experimental set-up, measurement techniques, and data analysis methodologies including velocity triple decomposition and the approach for estimating turbulent dissipation rate. In § 3, we provide a detailed analysis of wave classification for our measurement conditions. By synthesizing data from the literature, we propose a new dimensionless description of the wave classification. Section 4 describes the measured velocity fields and key turbulent parameters including turbulent intensities and Reynolds shear stress. We also evaluate the wave-induced flow field and the associated shear stress. In § 5, we present the TKE budget terms by phase-averaging, providing insights into the wave-coherent turbulence production, transport and dissipation. The detailed TKE budget analysis is also provided in § 5. Lastly, § 6 summarizes the findings and concluding remarks.

2. Experimental set-up and methods

2.1. *Experimental set-up in the wind-wave flume*

The wind-wave experiment was conducted within the wind-wave-current flume housed in the Environmental Fluid Dynamics Laboratory at Texas A&M University. The flume is

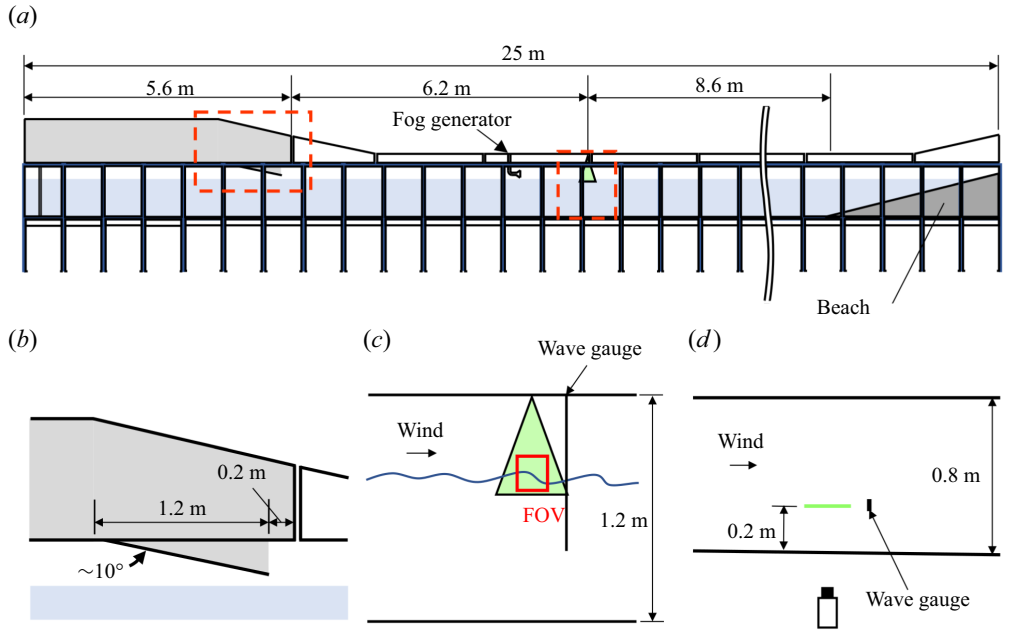

Figure 1. (*a*) Schematics of the wind-wave-current flume. The measurements of velocities and waves are at a fetch of 6.2 m downstream the wind-entrance-point at 5.6 m from the flume head. The nozzle of the fog generator was placed approximately 1.5 m upwind the measurement location for particle seeding. (*b*) A wind blower guide equipped with an angle of approximately 10°. (*c*) Side view of the measurement area. A wave gauge was placed 0.16 m downstream the measurement location. (*d*) Top view of the measurement area. The laser sheet is aligned at 0.2 m from the front side wall.

25 m long, 0.8 m wide and 1.0 m deep, and its schematic is shown in figure 1(*a*). When generating wind, the flume is enclosed by detachable covers with a height of 0.2 m on the top, making the height inside flume to be 1.2 m. A computer-controlled wind simulation system, located near the upwind end, is equipped on the top of the tank and can generate wind in the range of 0–20 m s^{-1}. The wind blows out into the flume at approximately 5.6 m from the upwind end through a wind blower guide (figure 1*b*). A 1:5 sloping beach with two layers of horsehair is placed to absorb the wave energy at the downwind end of the flume. A constant water depth of 0.80 m was maintained throughout the experiment. Three different wind speeds with their reference speeds measured at approximately 7 cm below the wind cap were used in the present study: $U_{ref} = 6.0$, 8.0 and 10.0 m s^{-1}. Above 10.0 m s^{-1}, breaking waves with air entrainment start to occur, which is beyond the scope of this study.

PIV was employed to measure the airflow above the wave surface at the fetch of 6.2 m and 0.2 m from the front wall. To obtain the wave information at the same time of the PIV measurements, a resistance-type wave gauge was placed approximately 16 cm downwind from the PIV measurement location to record the water surface elevation at 100 Hz while taking PIV images (figure 1*c*,*d*). After the completion of the PIV measurements, the wave gauge was moved to the PIV measurement location to record a 10-min wave dataset to obtain the wave parameters at the location of the PIV measurements for each wind speed.

2.2. *Particle image velocimetry*

A 15-W continuous-wave laser at 532 nm (Spectra-Physics, operated at 3 W) and a cylindrical lens were used to generate the PIV laser sheet. The airflow was seeded with

particles generated by a fog generator (SAFEX, Dantec) using SAFEX-Inside-Nebelfluid, a mixture of diethylene glycol and water, with a median particle diameter of approximately 1 μm. Particle relaxation time was estimated as $\tau_p = d_p^2 \rho_p / 18\mu_a \sim 3.2\,\mu s$, where d_p is the particle diameter ($d_p = 1\,\mu m$) and μ_a is the dynamic viscosity of air ($\mu_a = 1.8 \times 10^{-5}$ kg m^{-1} s^{-1}). With the estimated Kolmogorov time scale of 4.0, 2.8 and 1.9 ms for the three reference wind speeds, we calculated the Stokes number $St = \tau_p/\tau_\eta \sim O(10^{-3})$. Therefore, the seeding particles were well suited for flow-following in our PIV measurements.

The PIV images were acquired at a sampling rate of 2400 frames per second (fps) at a 12-bit dynamic range using a high-speed camera (Vision Research). The PIV FOV is 16.0×12.0 cm^2 with a spatial resolution of 0.125 mm pixel^{-1}. The camera was carefully adjusted so that air–water interface can be visualized in the images for later calculation of wave phase. A set of 6425 images (equivalently ∼2.7 s) were continuously recorded onto a camera with 12 GB of internal memory and then transferred to a computer for data processing. Five sets of data were recorded for each wind speed, which resulted in a total of 13.5 s of data for each case. Within this measurement duration, over 32 000 instantaneous flow fields were obtained over approximately 35–50 waves depending on the wind speed. The PIV images were processed using a commercial software package (DaVis, LaVision) with a search-and-interrogation window size of 128×128 and 32×32 pixel with a 50 % overlap, resulting in a normal resolution of equivalently 2.0×2.0 mm^2. Therefore, each pair of images resulted in 80×60 velocity vectors with a grid size of 2.0 mm in both x and z directions.

To obtain the water surface from the PIV images, an edge detection technique was applied because a strong light intensity gradient can be observed as a result of laser light reflection at the air–water interface (Reul, Branger & Giovanangeli 2008; Shaikh & Siddiqui 2010). A Hilbert transform was then used to determine the phase of the overlying flow field (Melville 1983; Buckley & Veron 2016; Porchetta *et al.* 2022). An example of the PIV velocity field and the wave phase are shown in figure 2 to demonstrate the instantaneous flow field and the associated vortex structure downstream of the wave crest. Note that the coordinate system is defined as the x direction begins at the left edge of the FOV and the z direction points upwards from the mean free surface elevation.

2.3. *Surface elevation measurements*

An example of a time series of water surface elevation shows that the wave height, length and period increase as the wind speed increases (figure 3, table 1). The power spectrum of the 10-min wave data is shown in figure 4, which is used to determine the dominant wave frequency f_p. The dominant wavelength λ_p and dominant wave speed c_p ($= \lambda_p f_p$) are then calculated based on linear wave theory. As expected, f_p decreases with the increase of wind speed. A secondary, wind speed-dependent peak is observed in each spectral plot, which may be attributed to a nonlinear interaction among waves. This secondary peak appears to be twice the peak frequency which has been observed in other wind-wave systems (Hidy & Plate 1966; Lake & Yuen 1978; Komen 1980). Table 1 summarizes important wave parameters, including the root-mean-square wave height H_{rms} and wave amplitude a_{rms}, the wave steepness $k_p a_{rms}$ ($k_p =$ the dominant wave number), and the significant wave height H_s. Other flow related parameters and dimensionless parameters including bulk Reynolds number, roughness Reynolds number, wave Reynolds number and Bond number are also reported in table 1.

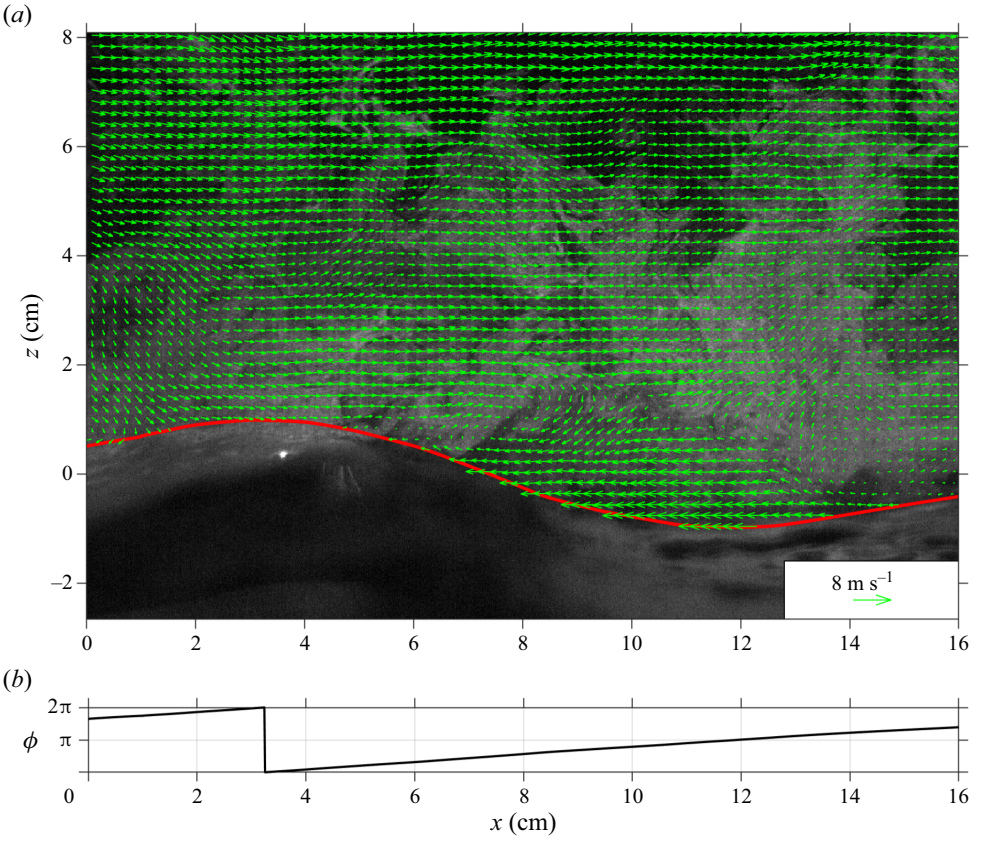

Figure 2. (*a*) An example of instantaneous velocity field measured using the PIV technique at $U_{ref} = 10.0$ m s^{-1}. The horizontal velocities were subtracted by half of the reference velocity to illustrate vortex features. The red curve indicates the detected air–water interface. (*b*) Detected phase using Hilbert transform along the free surface.

2.4. *Velocity triple-decomposition*

The instantaneous velocity vector $\boldsymbol{u}$ from the PIV measurements in the Cartesian coordinate system was decomposed into the phase-averaged velocity $\langle \boldsymbol{u} \rangle$ and turbulent fluctuating velocity $\boldsymbol{u}'$, while the phase-averaged velocity can be further decomposed into the time-averaged velocity $\bar{\boldsymbol{u}}$ and the wave induced velocity $\tilde{\boldsymbol{u}}$ (Hsu *et al*. 1981), i.e.

$$\boldsymbol{u}(x, z, t) = \langle \boldsymbol{u} \rangle (x, z) + \boldsymbol{u}'(x, z, t), \tag{2.1}$$

$$\langle \boldsymbol{u} \rangle (x, z) = \bar{\boldsymbol{u}}(z) + \tilde{\boldsymbol{u}}(x, z), \tag{2.2}$$

where $\boldsymbol{u} = (u,\ w)$ is the instantaneous velocity with u and w being the horizontal and vertical velocity components in the x and z directions, respectively. Since the two-dimensional PIV technique has been applied, no measurements on spanwise velocity v are available.

The phase-averaged and the time-averaged velocities were computed in the wave following coordinate system where $\zeta = 0$ denotes the wavy water surface. The wave-induced component was then converted back onto the Cartesian coordinate system to determine the turbulent velocities. Therefore, the wave-induced and turbulent velocity components are resolved as a function of phase in the Cartesian coordinate system in the

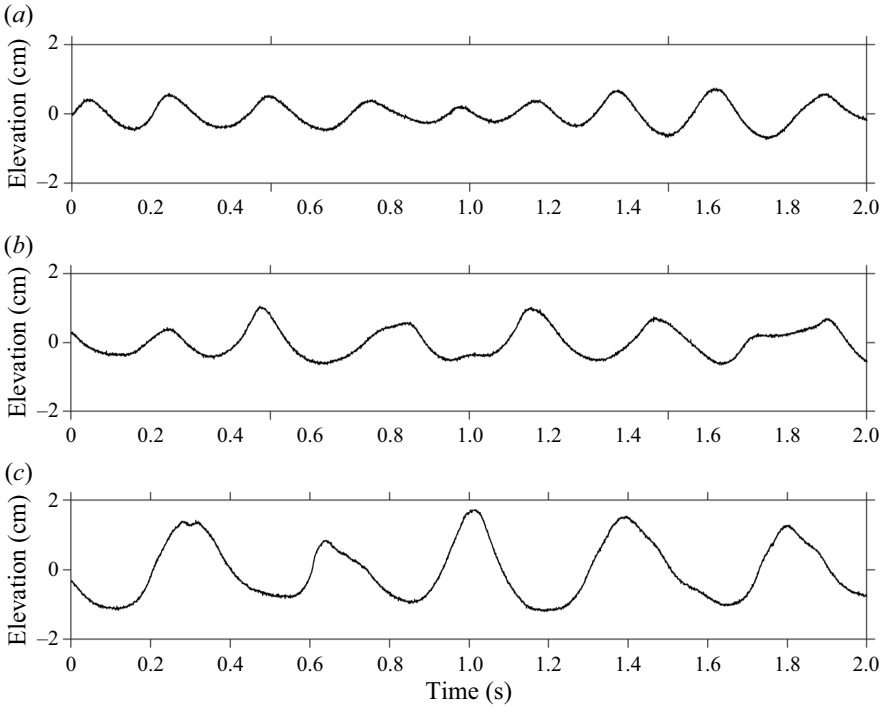

Figure 3. Examples of water surface elevations measured using the wave gauge for: (*a*) $U_{ref} = 6.0$ m s^{-1}; (*b*) $U_{ref} = 8.0$ m s^{-1}; (*c*) $U_{ref} = 10.0$ m s^{-1}.

Wind parameters	U_{ref} (m s^{-1})	6.0	8.0	10.0
	U_{10} (m s^{-1})	10.2	12.2	14.1
	u_* (m s^{-1})	0.38	0.44	0.50
	z_0 (mm)	0.218	0.163	0.112
Wave parameters	f_p (Hz)	4.0	3.2	2.9
	λ_p (m)	0.10	0.15	0.19
	c_p (m s^{-1})	0.39	0.49	0.54
	H_{rms} (m)	0.007	0.011	0.017
	H_s (m)	0.010	0.018	0.026
	k_p (m^{-1})	64	41	33
Dimensionless parameters	$k_p a_{rms}$	0.21	0.23	0.29
	c_p/u_*	1.03	1.10	1.09
	Re_D	158,300	211,100	263,900
	Re_0	5.47	4.75	3.67
	Re_w	38,100	73,900	99,700
	Bo	32	79	117

Table 1. Summary of the parameters. Reference velocity U_{ref}, 10 m equivalent velocity U_{10}, shear velocity of air u_*, roughness length z_0, spectral peak frequency f_p (obtained from wave power spectra shown in figure 2) and corresponding peak wavelength λ_p (calculated based on linear wave theory) and peak wave speed c_p (= $\lambda_p f_p$), root-mean-squared wave height H_{rms}, significant wave height H_s, peak wavenumber k_p (= $2\pi/\lambda_p$), peak wave steepness $k_p a_{rms}$ with a_{rms} being the wave amplitude, bulk Reynolds number $Re_D = U_{ref} D/\nu_a$ with D being the channel height and ν_a the kinematic viscosity of air, roughness Reynold number $Re_0 = u_* z_0/\nu_a$ based on the shear velocity of air and roughness length, wave Reynolds number $Re_w = c_p \lambda_p/\nu_w$ based on wave properties with ν_w being the kinematic viscosity of water, and Bond number $Bo = (\rho_w - \rho_a) g/(\sigma k_p^2)$ with ρ_w being the water density, ρ_a air density, g gravitational acceleration and σ surface tension.

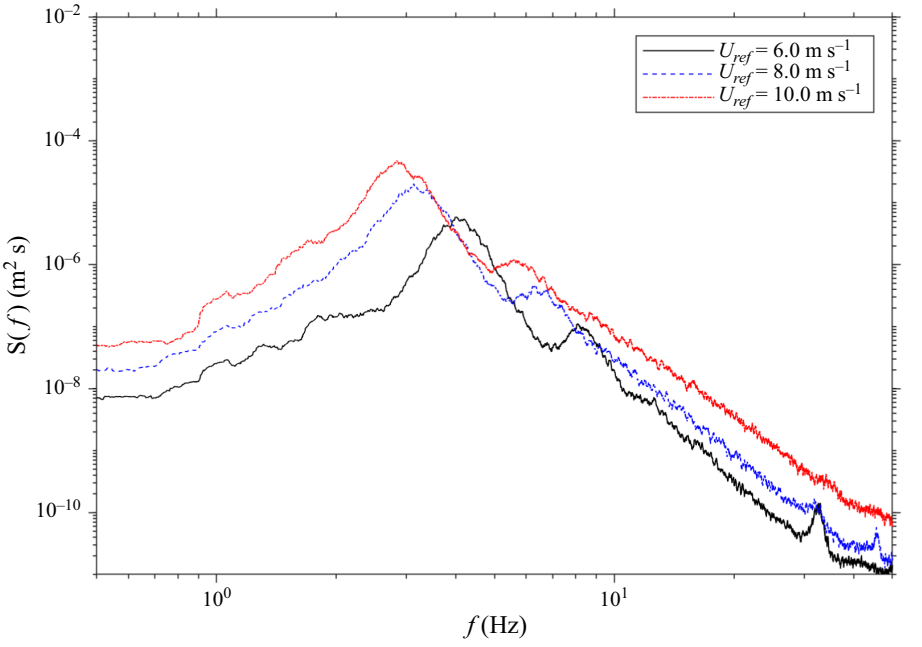

Figure 4. Power spectrum of water surface elevation determined from the wave gauge data.

presence of waves. Figure 5 shows an example of velocity triple-decomposition into the time-averaged, wave-induced and turbulent velocity components at $U_{ref} = 6.0$ m s^{-1}. In the horizontal direction (figure 5*a*), we observe a classic boundary layer profile of the mean flow, an organized, phase dependent wave-induced velocity field and a turbulent flow field which also show a somewhat organized pattern close to the water surface. In the vertical direction (figure 5*b*), there seems to be a mean downward flow within the measurement location, with decreasing velocity towards the water surface but changing the direction within the wave height. Again, the wave-induced velocity is highly phase dependent and the turbulent fluctuations are relatively chaotic.

2.5. *Estimation of turbulent dissipation rate*

To obtain the spatial distribution of turbulent dissipation rate, ε, a 'direct method' can be applied for PIV measurements (Luznik *et al*. 2007; Wang & Liao 2016). The technique is based on the resolved velocity gradient from the PIV data, the continuity equation and necessary assumptions of local isotropy in small scales. The directly estimated turbulent dissipation rate reads:

$$\varepsilon_D^A = 4\nu \left\langle \left(\frac{\partial u'}{\partial x}\right)^2 + \left(\frac{\partial w'}{\partial z}\right)^2 + \frac{3}{4}\left(\frac{\partial u'}{\partial z}\right)^2 + \frac{3}{4}\left(\frac{\partial w'}{\partial x}\right)^2 + \left(\frac{\partial u'}{\partial x}\frac{\partial w'}{\partial z}\right) + \frac{3}{2}\left(\frac{\partial u'}{\partial z}\frac{\partial w'}{\partial x}\right)\right\rangle. \quad (2.3)$$

From the two-dimensional PIV data, this method provides an instantaneous turbulent dissipation rate, which can be ensemble-averaged to obtain the phase-dependent ε for illustrating the wave effect. However, this method suffers from the coarse spatial resolution when the resolved spatial resolution is more than one order of magnitude larger than the Kolmogorov length scale (Saarenrinne & Piirto 2000; Luznik *et al*. 2007; Xu & Chen 2013). In contrast, the velocity spectrum remains quite robust even with coarse spatial

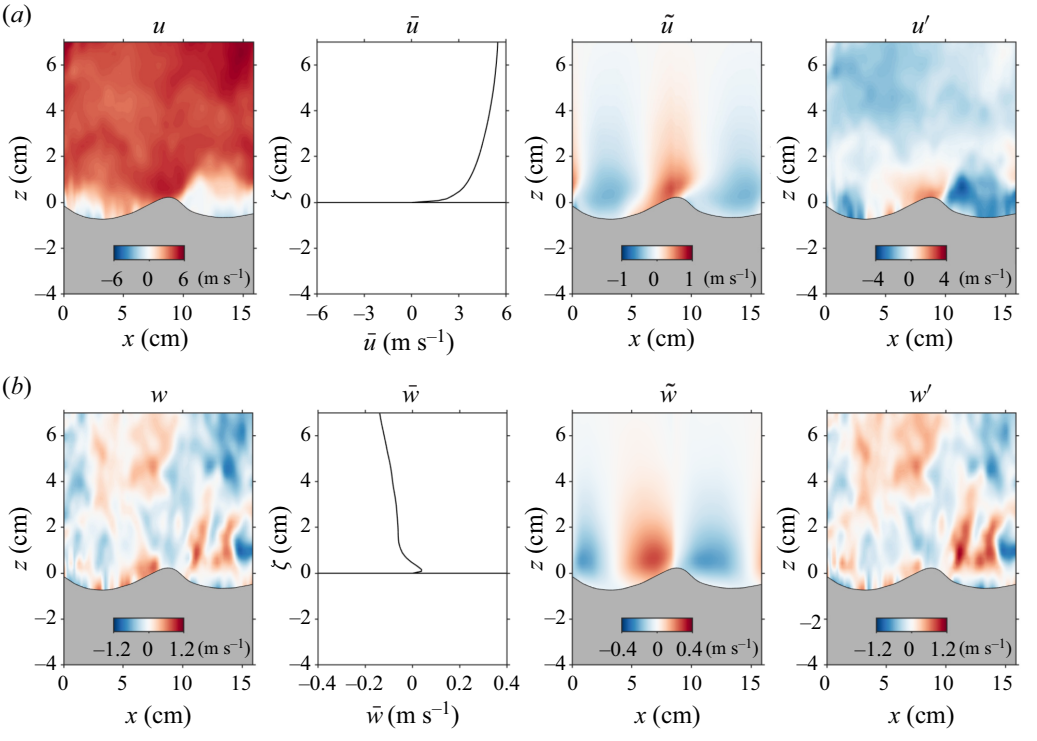

Figure 5. An example of velocity triple decomposition at $U_{ref} = 6.0$ m s^{-1}. (*a*) Horizontal velocity fields: instantaneous u, time averaged mean $\bar{u}$, wave induced mean $\tilde{u}$ and turbulent velocity u'. (*b*) Vertical velocity fields: instantaneous w, time averaged mean $\bar{w}$, wave induced mean $\tilde{w}$ and turbulent velocity w'. Note that the wind blows from left to right and there is variation present on the contour colour bars from panel to panel.

resolution (Xu & Chen 2013), such that ε can be estimated reliably by fitting the spectrum to the universal Kolmogorov $-5/3$ law in the inertial subrange (Tennekes & Lumley 1972):

$$E(k) = \frac{18}{55}\beta\varepsilon^{2/3}k^{-5/3}, \tag{2.4}$$

where $E(k)$ is the energy spectral density of the one-dimensional streamwise velocity determined in the main flow direction of the wavenumber domain, $\beta = 1.6$ is the universal Kolmogorov constant (Doron *et al.* 2001) and k is the wavenumber along the main flow direction.

In our time-resolved PIV measurements, the time-series data of instantaneous velocity at any given location above the height of wave crest can be used to calculate the energy spectral density in the frequency domain $E(f)$, which can be converted to $E(k) = (U/2\pi)E(f)$ by revoking the Taylor's frozen turbulence hypothesis, where the frequency $f = (U/2\pi)k$ and U is the mean streamwise velocity (Li *et al.* 2023).

Figure 6(*a*) presents one-dimensional streamwise velocity spectra at several z values in the wavenumber domain, obtained by converting from the frequency domain. At measurement locations within the range of 0.03–0.08 m where the length scale of turbulent eddies in the vertical direction is constrained by the water surface, we observed a clearly defined $-5/3$ slope in the range of 30–200 rad m^{-1}, corresponding to eddy sizes of approximately 0.03–0.2 m. This suggests that a pronounced $-5/3$ slope can be observed in the range above the resolved largest length scale in the vertical direction. While turbulence eddies are typically isotropic in the inertial subrange, our findings indicate that the $-5/3$

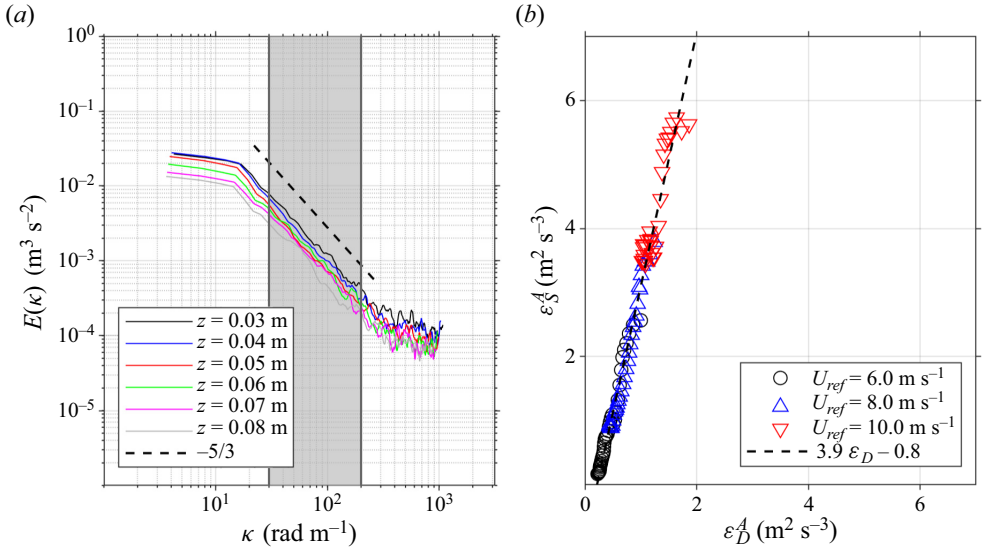

Figure 6. (*a*) One-dimensional velocity spectra in the horizontal wave number domain for the case of $U_{ref} = 10.0$ m s^{-1} wind. The spectrum was converted from that in the frequency domain, which was computed from the time-series data. The shaded region indicates the inertial subrange where the −5/3 universal scaling law was applied to estimate turbulent dissipation rate. (*b*) Comparison of turbulence dissipation rate estimate using the spectrum and direct method above the maximum wave height for all three reference wind speeds. The dashed line is the linear fit.

slope in the streamwise velocity spectra deviates somewhat from the isotropic expectation, suggesting a degree of relaxation. However, we note that one-dimensional vertical velocity spectra are suppressed by the constraint in the resolved turbulent eddy sizes.

After the inertial subrange was identified, regression can then be applied using (2.4) to estimate the turbulent dissipation rate. This method provides the time-averaged turbulent dissipation rate, denoted as ε_S^A, above the wave crest over the entire measurement period and across all phases of wind waves. Fitting the velocity spectrum at different heights allows for the estimation of a vertical profile of turbulent dissipation rate. If the profile of ε_S^A represents the unbiased estimate of turbulent dissipation rate, we can use this profile as a benchmark to correct underestimation caused by the coarse spatial resolution in the 'direct method' (Johnson & Cowen 2018; Wu *et al.* 2021).

We calculated the vertical profile of ε_D^A by averaging it on the same coordinate as that for ε_S^A. Therefore, the two vertical profiles can be directly compared, as shown in figure 6(*b*). The data indicate that ε_D^A is smaller than ε_S^A at almost all heights and underestimate the turbulent dissipation rates as expected. Using $\varepsilon_S^A = 0.9$, 1.9 and 4.2 m^2 s^{-3} for an averaged value in the measurement region, the Kolmogorov length scales are estimated to be $\eta = (\nu_a^3/\varepsilon)^{1/4} = 0.25$, 0.20 and 0.17 mm, for $U_{ref} = 6.0$, 8.0 and 10.0 m s^{-1}, respectively. Hence, the ratio of PIV resolved spatial resolution to the Kolmogorov length Δ/η is 8.1, 9.8 and 11.8, respectively. Saarenrinne & Piirto (2000) showed the errors in dissipation rate falls more than 90 % when $10 < \Delta/\eta < 15$, while Xu & Chen (2013) also estimated that dissipation rate using velocity gradients can be less than 25 % of the true dissipation rate when $\Delta/\eta < 14$. The linear regression was used to find the relationship between the two methods: $\varepsilon_S^A = 3.9\varepsilon_D^A - 0.8$ (figure 6*b*). The factor of 3.9 agrees with the expected underestimation given the range of Δ/η in this study (Saarenrinne & Piirto 2000; Xu & Chen 2013).

Category	Classifications	λ_p (cm)	Bo	Re_*
I	Capillary waves dissipated by molecular viscosity	<4	<5	$<3.74 \times 10^4$
II	Gravity-capillary waves dissipated by generation of capillaries	4–10	5–34	3.74×10^4–1.19×10^5
III	Gravity-capillary waves dissipated by generation of capillaries and microscale breaking	10–20	34–134	1.19×10^5–2.85×10^5
IV	Short gravity waves dissipated by generation of macro- and microscale breaking	>20	>134	$>2.85 \times 10^5$

Table 2. Flow regime based on dominant wavelength λ_p proposed by Caulliez (2013), corresponding Bond number Bo and the shear-fetch based Reynolds number Re_* ($= u_*F/\nu_a$), based on the shear velocity of air and fetch length.

Once the spatial distribution of instantaneous turbulent dissipation rate was estimated using the 'direct method', we follow the same procedure as in other mean flow and turbulent quantities to determine their phase-averaged values.

3. Classification of wind waves

3.1. *Classification using dominant wavelength*

Caulliez (2013) classified the wind waves into four categories, depending on the dissipation mechanism of surface waves: (1) capillary waves dissipated by molecular viscosity (category I); (2) gravity-capillary waves dissipated by generation of capillaries (category II); (3) gravity-capillary waves dissipated by generation of capillaries and microscale breaking (category III); and (4) short gravity waves dissipated by generation of micro- and macroscale breaking (category IV). Furthermore, Caulliez (2013) proposed a simple criterion based on dominant wavelength using the data from a wind-wave flume over the wind speed of 2.5–12 m s^{-1} and fetch of 2–26 m (table 2).

To demonstrate the wave classification and flow regime under these waves, we summarized our data along with available data of similar wind waves in laboratory scales, including those of Toba (1972), Siddiqui & Loewen (2007) and Caulliez (2013), in figure 7. Multiple groups of near-linear relationship are shown in the log–log plot of wavelength as a function of the shear velocity of air (figure 7*a*). Each group corresponds to a different fetch either within the same wave tank or across different studies. Not surprisingly, the data show that both wind shear and fetch correlate positively to the dominant wavelength. Regression of each data group results in an averaged slope of 0.98 in the log–log plot, suggesting a near-linear relationship between wavelength and the shear velocity.

To account for the combined effects of wind shear and fetch, we plot the dominant wavelength against the quantity $u_*^{5/4}F$ (figure 7*b*), an alternative of $U_\infty^{5/4}F$ which is proposed by Lamont-Smith & Waseda (2008) to characterize the wave frequency $f_p \propto (U_\infty^{5/4}F)^{-0.43}$, where U_∞ is the mean velocity measured 50 cm above the still water surface in their experiments. The shear velocity u_* was obtained from log-law fitting to the mean velocity profile above the wind waves (see § 4.1). We found that using the quantity $u_*^{5/4}F$ is an effective approach to combine wave and fetch in characterizing the

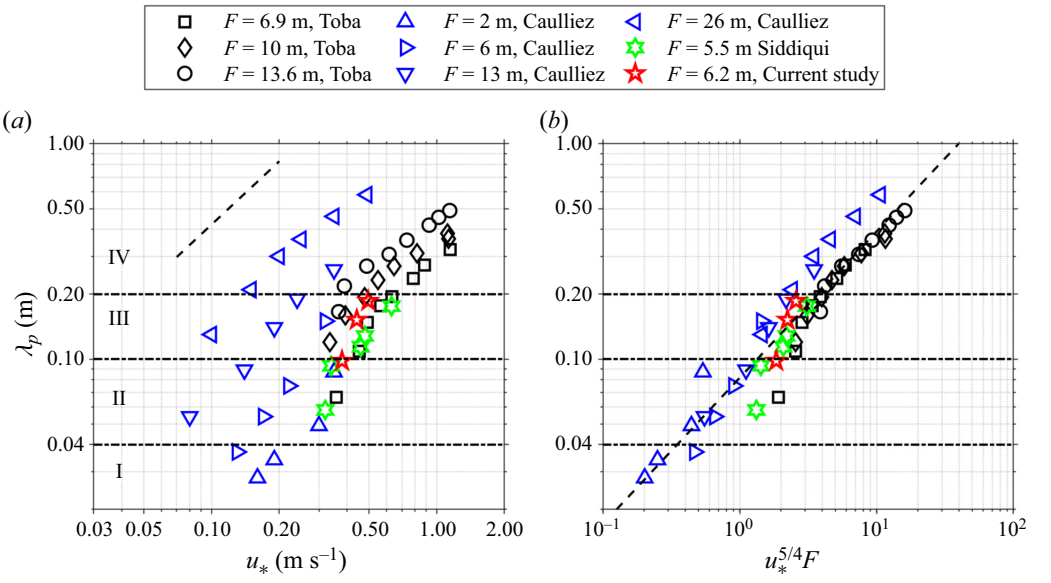

Figure 7. (*a*) Comparison between dominant wavelength λ_p and the shear velocity of air u_* with data from Toba (1972), Siddiqui & Loewen (2007) and Caulliez (2013). The four flow regimes are marked based on the wavelength criterion (Caulliez 2013, table 2). The slope of the dashed line is 0.98, which is the averaged slope over the different data groups. (*b*) Comparison between λ_p and $u_*^{5/4}F$. The dashed fitted line is $\lambda_p = 0.082(u_*^{5/4}F)^{2/3}$ with an R^2 value of 0.90.

dominant wavelength in various laboratory studies. The best-fit relationship across the range of laboratory wind and fetch data gives $\lambda_p = 0.082(u_*^{5/4}F)^{2/3}$.

The data show that our wind wave conditions fall primarily within the category III (figure 7). The case of $U_{ref} = 6.0$ m s^{-1} is near the boundary between categories II and III, and the case of $U_{ref} = 10.0$ m s^{-1} is near the boundary of III and IV. This indicates the micro-scaling breakings started to form at $U_{ref} = 6.0$ m s^{-1}, but the surface was primarily covered by capillaries. For $U_{ref} = 10.0$ m s^{-1}, macroscale breaking was about to form on the water surface while the water surface was covered by microscale breaking. Direct visualization of water surface morphology (figure 8) supports the classification using the dominant wavelength. For $U_{ref} = 6.0$ m s^{-1}, water surface on the windward side of crest is mainly occupied by a smooth surface, while ripples are observed close to the crest and on the leeward side, known as parasitic capillaries which are commonly observed on short wind-wave surfaces (Cox 1958; Zhang 1995). With increasing wind speed, surface roughness increases and the formation of parasitic capillaries is intensified. For $U_{ref} = 8.0$ m s^{-1}, a small portion of water surface may still be considered smooth. For $U_{ref} = 10.0$ m s^{-1}, the water surface is completely covered by capillaries and rollers, i.e. microscale breakers. Further increasing wind speed will lead to air-entraining breaking, which was visually confirmed. Similar observations were also made by Toba (1961) who reported that the lowest reference wind speeds for the occurrence of the air entrainment in wind waves were approximately 10.8 and 9.7 m s^{-1} at fetches of 5.5 and 7.0 m, respectively. Loewen & Siddiqui (2006) and Siddiqui & Loewen (2007) quantified that the breaking percentage increased from 11 % to 80 % as the wind speed increases from 4.5

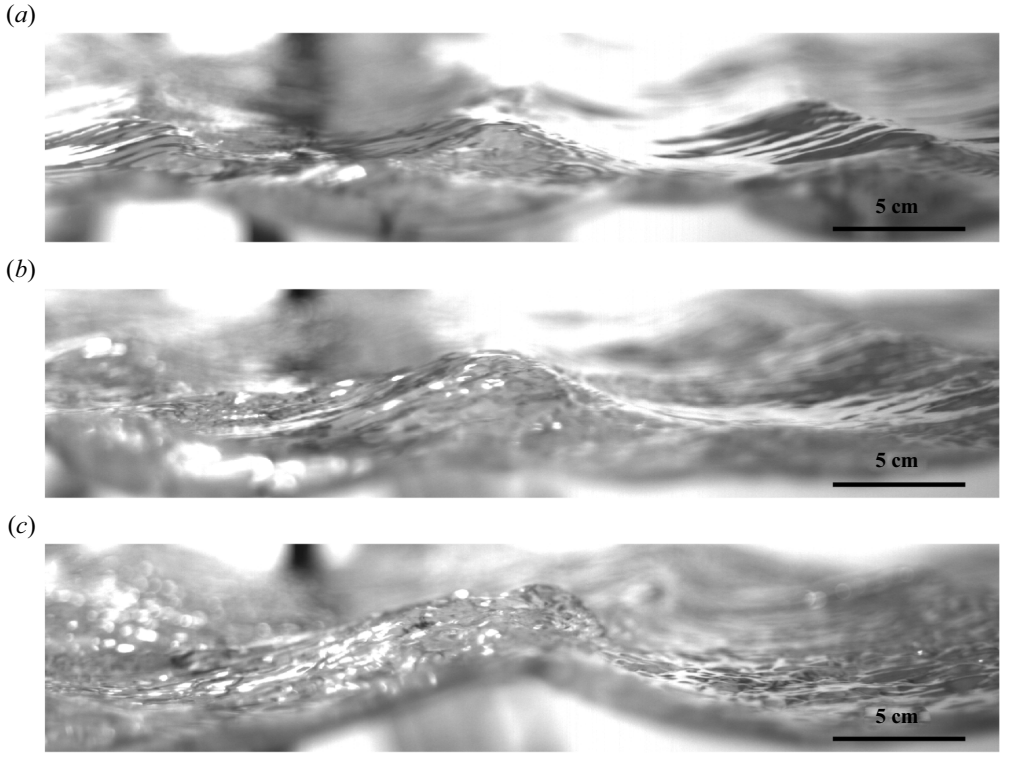

Figure 8. Sample images of wind generated waves: (*a*) $U_{ref} = 6.0$ m s^{-1}; (*b*) $U_{ref} = 8.0$ m s^{-1}; (*c*) $U_{ref} = 10.0$ m s^{-1}. Note that the wind blows from left to right.

to 7.4 m s^{-1} and increased to 90 % at 11 m s^{-1} by detecting micro-breaking waves at a fetch of 5.5 m.

3.2. *Dimensionless parameters*

One shortcoming of the above wave classification is that all parameters are evaluated in the physical space, which hinders its application across different measurements. To explore using dimensionless parameters in classifying wind waves, the Bond number has been proposed instead of the dominant wavelength (Deike, Popinet & Melville 2015; Wu & Deike 2021): $Bo = (\rho_w - \rho_a)gL^2/\sigma$, where ρ_w is water density, ρ_a is air density, g is gravitational acceleration, σ is surface tension and L is the characteristic length scale. In the present study, L is related to the wavelength through wavenumber k_p as $L = 1/k_p$, where $k_p = 2\pi/\lambda_p$. Because the only varying parameter in Bo is the wavelength in the air–water systems, the classification based on wavelength can be directly converted into a Bond number-based classification.

Here we seek to understand how Bond number can be scaled using dimensionless parameters that are related to wind and waves, so that wind waves can be directly classified using wind and wave parameters in the non-dimensional space. To incorporate shear velocity and fetch in the scaling, we test two dimensionless numbers: shear-fetch based Froude number $Fr_* = u_*/\sqrt{gF}$ and shear-fetch based Reynolds number $Re_* = u_*F/\nu_a$ (Wu 1971, 1973). The relationships of Bo versus Fr_* and Bo versus Re_* are plotted in figure 9, including the data from Toba (1972), Siddiqui & Loewen (2007), Caulliez (2013)

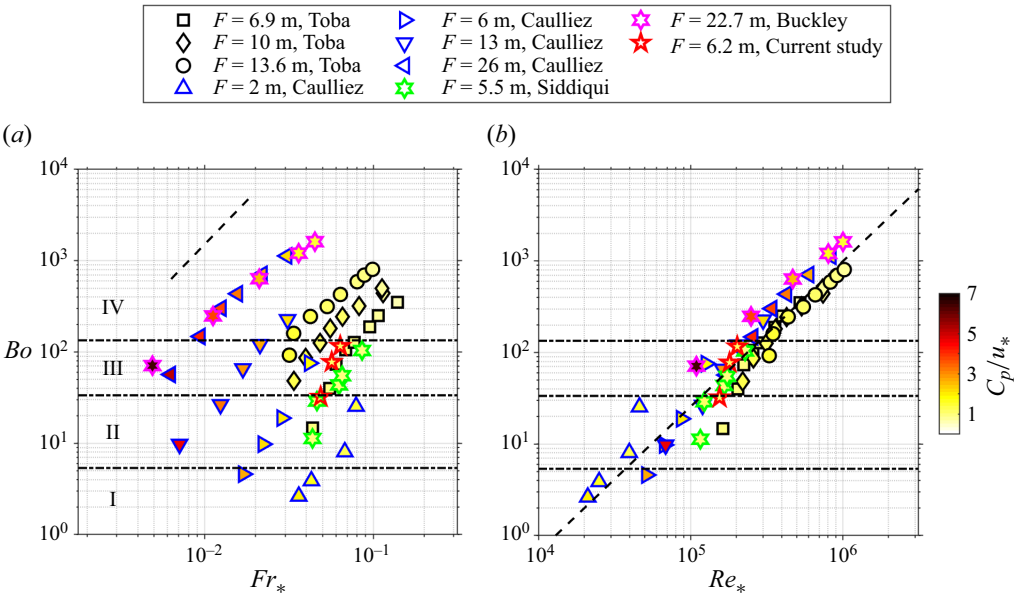

Figure 9. Flow regimes in the space of dimensionless parameters. Data include the present study, and those from Toba (1972), Siddiqui & Loewen (2007), Caulliez (2013) and Buckley & Veron (2016). (*a*) Shear-fetch based Froude number Fr_* versus Bond number Bo. The dashed line indicates the averaged slope of 1.91 over the different data groups. (*b*) Shear-fetch based Reynolds number Re_* versus Bond number Bo. The dashed fitting line is $Bo = 3.02 \times 10^{-7} Re_*^{8/5}$ with an R^2 value of 0.91. Note that the fill colour of each data point is coded with wave age c_p/u_* according to the colour bar, while the symbol outline colour is coded as given in the legend at the top.

and Buckley & Veron (2016). The plots in figure 9 are colour-coded using the wave age c_p/u_* to illustrate the effect of wave age on the wave classification. Similar to figure 7(*a*), the data show groups of linear trends in Bo versus Fr_* on the log–log scale (figure 9*a*). The slopes of each line are averaged to be 1.91, giving $Bo \propto Fr_*^{1.91}$. Examining all data, we found that wave age is not an influential factor in Bond number-based classification of wind waves as it appears uncorrelated with Bo. However, the relationship of Bo versus Re_* shows that Re_* can universalize the combined effect of wind shear and fetch across the range of available data and the regression suggests $Bo \propto Re_*^{8/5}$ (figure 9*b*). Based on the classification thresholds using dominant wavelength proposed by Caulliez (2013), we estimated the thresholds of Bo and Re_* to classify wind waves (table 2). The wind waves in categories I, II and IV are consistent with the wave shapes of nonlinear capillary waves, parasitic capillary waves, and spilling breakers for $Bo = 1.47$, 25 and 200, respectively, throughout numerical simulation (Wu & Deike 2021). With the dimensionless parameterization, the proposed new classification can be easily applied to other studies, but it needs to be validated in the future.

4. Velocity fields and stresses

4.1. *Mean velocity*

The horizontal velocity profiles averaged over the measurement duration and over all phases show a logarithmic shape similar to those in wall boundary flows (figure 10*a*).

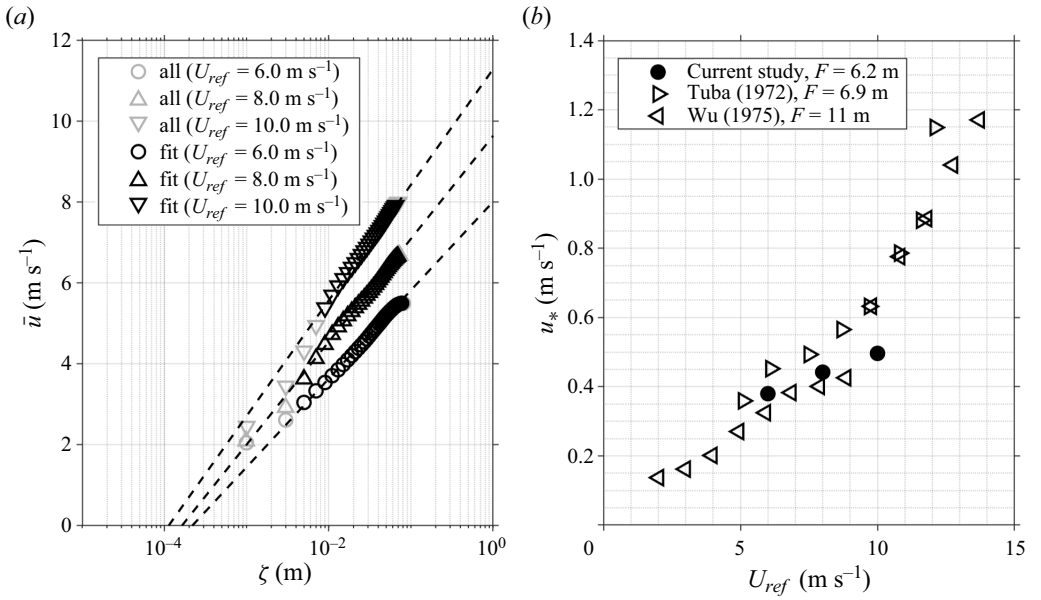

Figure 10. (*a*) Profiles of mean horizontal velocity $\bar{u}$ above the wave surface and the regression lines using law-of-the-wall equation; (*b*) shear velocity u_* determined from the law-of-the-wall regression as a function of U_{ref}. Data include those from Toba (1972) and Wu (1975) at a fetch of 6.9 and 11 m, respectively.

We consider the wave boundary as a quasi-stationary feature at the measurement location, so that the mean velocity profile averaged in the wave-following coordinate can be compared with that in wall bounded turbulent flows. To estimate the wind parameters, including shear velocity, 10 m equivalent velocity and roughness length over the water surface, we used the standard law-of-the-wall (LOW) fitting and selected data points for fitting based on a goodness-of-fit criterion, i.e. $R^2 > 0.9$. The results of the LOW fitting are summarized in table 1. The fitted shear velocities are positively correlated with the wind speed, and the data are consistent with those reported in the literatures for similar laboratory wind wave measurements, such as 6.9 m fetch by Toba (1972) and 5.5 m fetch by Siddiqui & Loewen (2007) (figure 10*b*).

Based on the measured wind shear and wave parameters, the range of wave ages ($c_p/u_* = 1.03$–1.10) indicates that the wave fields in this study are young developing waves (Sullivan & McWilliams 2010). Unlike previously reported numerical and experimental results that cover a wide range of wave ages (e.g. Rutgersson & Sullivan 2005; Yang & Shen 2010; Buckley & Veron 2016), this study focuses on a narrow range of wave ages but various stages of wave categories (i.e. capillary, microscale and macroscale breaking).

4.2. *Wave-induced velocity and stress*

The phase-averaged wave-induced velocities ($\tilde{u}$, $\tilde{w}$) and wave-induced stress (analogues of Reynolds shear stress, $-\langle\tilde{u}\tilde{w}\rangle$) show consistent spatial patterns above the wind waves for different wind speeds (figure 11). In general, $\tilde{u}/u_*$ is positive over the crest and negative over the trough. Away from the surface ($k_p z > \sim 0.5$), the positive $\tilde{u}/u_*$ region on the crest changes its direction from positive to negative on the leeward side of the crest ($x/\lambda_p = \sim 0.25$) and back to positive on the windward side of the crest ($x/\lambda_p = \sim 0.75$).

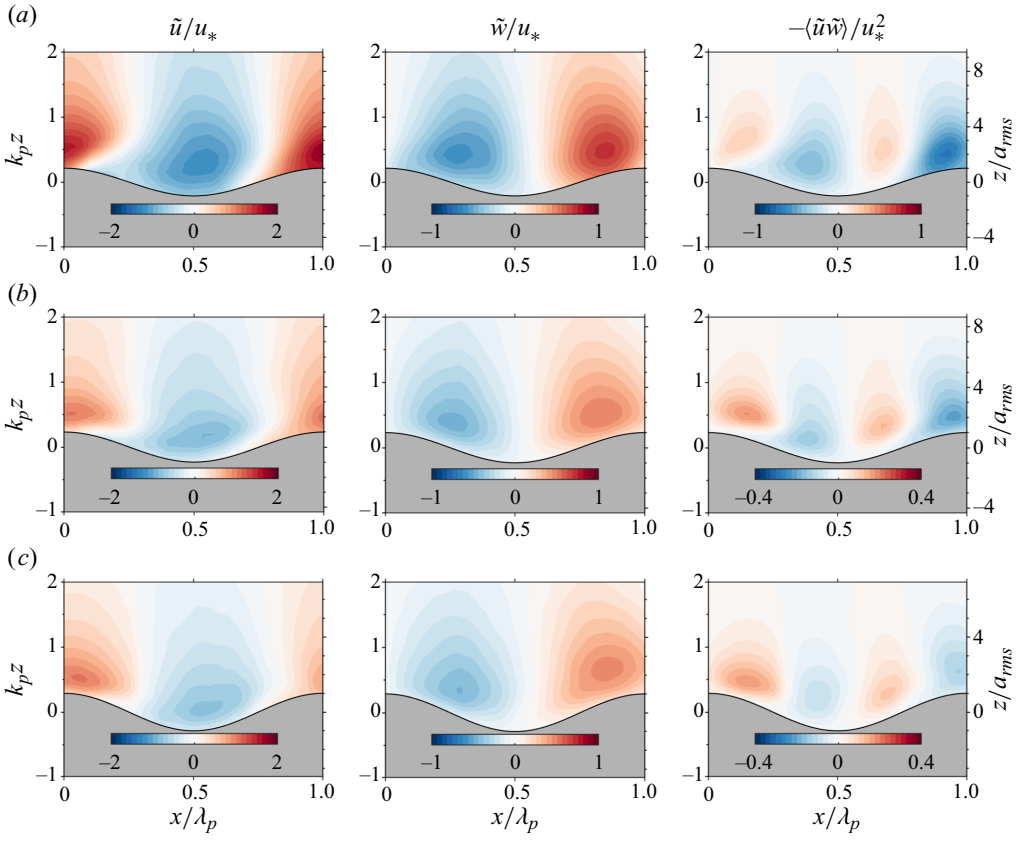

Figure 11. Phase-averaged normalized wave-induced velocities and wave-induced stress, i.e. $\tilde{u}/u_*$, $\tilde{w}/u_*$ and $-\langle\tilde{u}\tilde{w}\rangle/u_*^2$ at: (*a*) $U_{ref} = 6.0$ m s^{-1}; (*b*) $U_{ref} = 8.0$ m s^{-1}; (*c*) $U_{ref} = 10.0$ m s^{-1}. Note that the wind blows from left to right and there is variation present on the contour colour bars from panel to panel.

Close to the surface ($k_pz < \sim 0.5$), the direction rapidly shifts passing the crest on the leeward side of the crest ($\sim 0.1 < x/\lambda_p < \sim 0.25$) and relatively smooth transition occurs on the windward side of the crest ($\sim 0.7 < x/\lambda_p < \sim 0.75$). Also, while the intensified positive $\tilde{u}/u_*$ region is located near $k_pz = \sim 0.5$ on the crest, the intensified negative region moves close to the surface on the trough with increasing wind speed. The pattern of $\tilde{u}/u_*$ suggests that the wave perturbation causes the airflow to accelerate over the wave crest and decelerate over the wave trough. The patterns are generally consistent with the available experimental results reported with wave age of 1.4 and 2.5 at a fetch of 22.7 m (Buckley & Veron 2019). In addition, the data show that the positive $\tilde{u}/u_*$ region on the leeward side extends towards the near surface region of the trough and the magnitude decreases with increasing wind speed.

Here, $\tilde{w}/u_*$ shows negative values on the leeward side and positive values on the windward side, a classic wave-induced velocity pattern above a wavy surface. Similar to $\tilde{u}/u_*$, the magnitude decreases with increasing wind speed, and the patterns are also consistent with a wave age of 1.4 and 2.5 (Buckley & Veron 2019). Examining the velocity in both horizontal and vertical directions, the wave effect can be interpreted as that the air flow accelerates above the crest with a downward velocity on the leeward side. The flow then moves upwards on the windward side and decelerates above the trough.

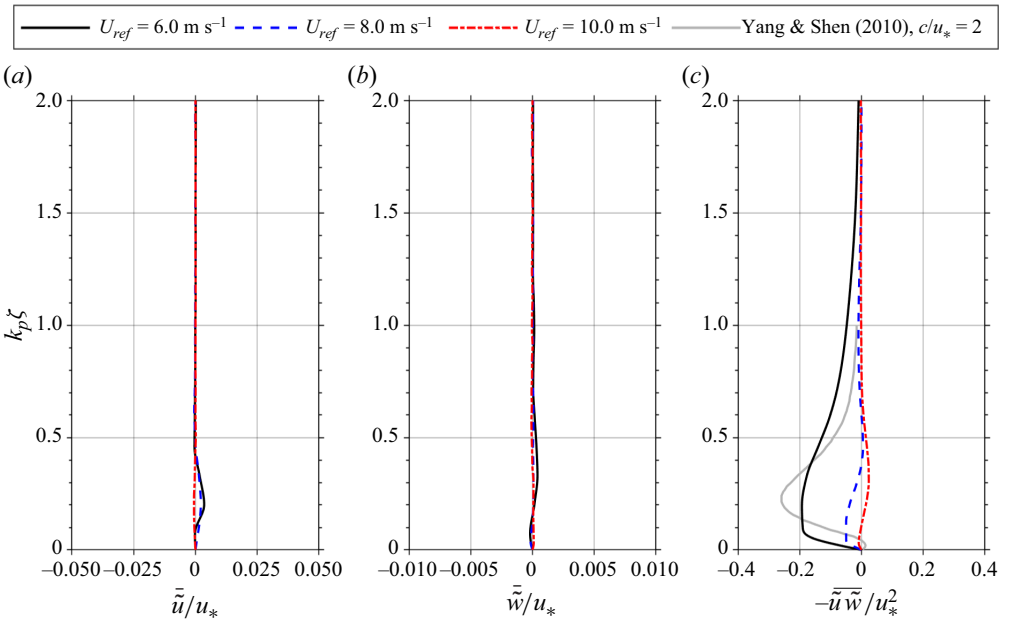

Figure 12. Vertical profiles of normalized: (*a*) horizontal wave-induced velocities $\tilde{\bar{u}}/u_*$; (*b*) vertical wave-induced velocities $\tilde{\bar{w}}/u_*$; and (*c*) wave-induced stresses $-\tilde{\bar{u}}\tilde{\bar{w}}/u_*^2$.

The pattern of $-\langle\tilde{u}\tilde{w}\rangle/u_*^2$ can be explained by the shear flow relative to the mean flow induced by the wave perturbation as indicated above. In the main flow field away from the water surface, $-\langle\tilde{u}\tilde{w}\rangle/u_*^2$ is positive near crest on the leeward side and near trough on the windward side, while is negative near trough on the leeward side and near crest on the windward side. Similar to $\tilde{u}/u_*$, near the surface, the positive $-\langle\tilde{u}\tilde{w}\rangle/u_*^2$ region on the leeward side extends towards the near surface region of the trough. The positive $-\langle\tilde{u}\tilde{w}\rangle/u_*^2$ region, near the surface on the windward side, extends towards the near surface region of the crest.

Figure 12 shows the vertical profile of wave-induced velocities and stress over the course of one wavelength. The wave-induced velocities are negligibly small and wave-induced stress is confined within $k_p\zeta < \sim 1.5$, where ζ is the vertical coordinate in a wave-following system after phase-averaging, i.e. $\zeta = 0$ is the water surface. Away from the confined region, the wave-induced accelerating and decelerating stages of flow compensate for each other, resulting in a quasi-steady flow. The vertical profile of wave-induced stress seems to be quite sensitive to the changing wind speeds and wave stages, compared with the profiles of $\tilde{\bar{u}}/u_*$ and $\tilde{\bar{w}}/u_*$ in different cases. For the case of $U_{ref} = 6.0$ m s^{-1}, a negative peak appears near the water surface. A similar profile was also observed by Yang & Shen (2010) with the wave age of 2 (figure 12*c*). The magnitude of wave-induced stress decreases with increasing wind speed. Very different profiles of wave-induced stress were also observed by Yang & Shen (2010) with the wave age of 14 and 25 and by Buckley & Veron (2016) with wave ages of 3.7–31.7. They presented large positive values near the surface and very small negative values above, indicating that the wave-induced stress is influenced by the wave ages. However, as our wave ages are quite similar, we suspect that the wave surface morphology may also contribute to the variability of the wave-induced stress profiles, in addition to the wave age.

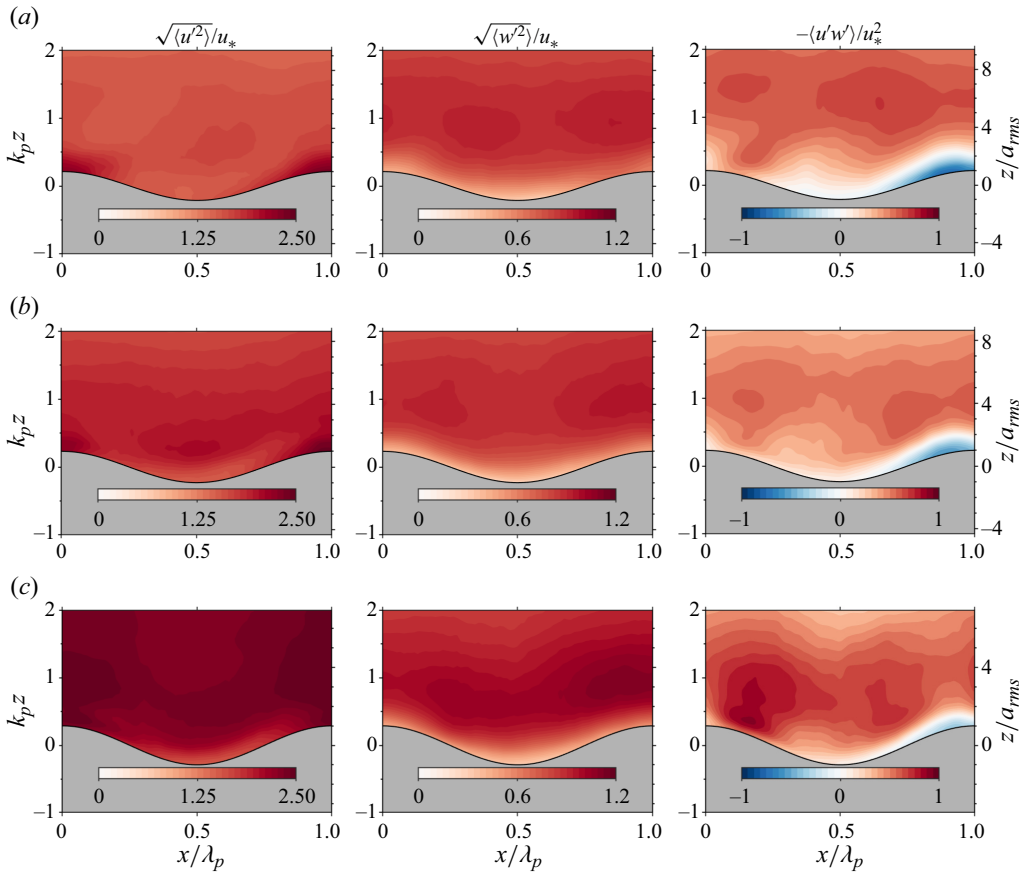

Figure 13. Phase-averaged normalized turbulent intensities and Reynolds shear stress, i.e. $\sqrt{\langle u'^2\rangle}/u_*$, $\sqrt{\langle w'^2\rangle}/u_*$ and $-\langle u'w'\rangle/u_*^2$ at: (*a*) $U_{ref} = 6.0$ m s^{-1}; (*b*) $U_{ref} = 8.0$ m s^{-1}; (*c*) $U_{ref} = 10.0$ m s^{-1}. Note that the wind blows from left to right.

4.3. *Turbulent intensity and Reynolds shear stress*

The spatial distribution of the phase-averaged turbulent intensities (i.e. square-root of Reynolds normal stresses) and Reynolds shear stress demonstrates the phase-independent velocity fluctuations and the associated momentum flux above the wavy water surface (figure 13). The data show that the variations of turbulent intensities over different phases of waves are quite small. The values of turbulent intensities are of the same order of the shear velocity, with the horizontal turbulent intensity approximately twice that of the vertical turbulent intensity.

Most of the flow field is covered by positive Reynolds shear stress (figure 13). Near the water surface, Reynolds shear stress decreases to close to zero. On the windward side immediately above the water surface, there appears a narrow region of negative Reynolds shear stress, which is likely attributed to the 'blocking' effect of the wavy water surface that moves slower than the air. Buckley & Veron (2019) also reported negative values over a narrow region on the windward side of the crest ($\sim 0.7 < x/\lambda_p < \sim 0.9$). In addition, they observed intensified positive Reynolds shear stress over a wide region on the leeward side ($\sim 0.1 < x/\lambda_p < \sim 0.4$). In our data, the intensified positive Reynolds shear stress on the

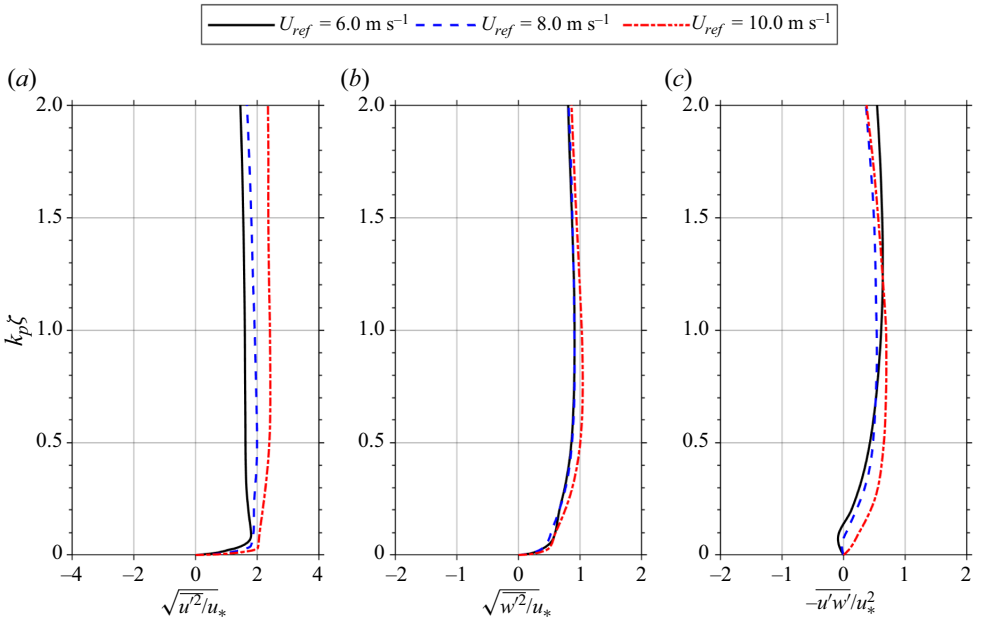

Figure 14. Vertical profiles of (*a*) horizontal turbulent intensities $\sqrt{\overline{u'^2}}/u_*$, (*b*) vertical turbulent intensities $\sqrt{\overline{w'^2}}/u_*$, (*c*) Reynolds shear stresses $-\overline{u'w'}/u_*^2$. All are normalized using shear velocity.

leeward side appears as more obvious in the case of $U_{ref} = 10.0$ m s^{-1}. The intensified Reynolds shear stress is one of the contributors to the strong shear production of TKE at this region (see figure 15). We note that the spatial pattern of the Reynolds shear stress in the wind-wave field is slightly different from that over a stationary wavy wall, where the maximum Reynolds shear stress is located on the trough ($x/\lambda_p = \sim 0.5$) and approximately the height of wavy surface, while the negative values lie on both windward and leeward sides (e.g. Hudson, Dykhno & Hanratty 1996; Yang & Shen 2010). The reason for the different spatial patterns between a stationary wavy wall and wind waves must result from the moving boundary, which leads to different slip boundary conditions.

The turbulent intensities and Reynolds shear stress over all phases show quite uniform vertical profiles for $k_p\zeta > \sim 0.5$ when averaged in the wave-following system (figure 14). Here, $\sqrt{\overline{u'^2}}/u_*$ increases slightly around the value of 2 with increasing wind speed, whereas $\sqrt{\overline{w'^2}}/u_*$ remains close to 1. Additionally, $-\overline{u'w'}/u_*^2$ seems to change its shape of profile at different wind speeds. For the case of $U_{ref} = 6.0$ m s^{-1}, $-\overline{u'w'}/u_*^2$ is almost constant with a value of ~ 0.7 at $k_p\zeta > \sim 0.5$. With increasing wind speed, $-\overline{u'w'}/u_*^2$ increases near the water surface at $k_p\zeta < \sim 1.2$, but decreases away from the water surface at $k_p\zeta > \sim 1.2$. The changing shape of Reynolds shear stress may be due to the changing roughness and the boundary layer thickness with increasing wind speed. The changing shape of Reynolds shear stress profile was also observed by Buckley & Veron (2019), who reported that the Reynolds shear stress increases with higher wind speed and lower wave age, while the thickness of the boundary layer gets thinner.

Comparing the wave-induced and turbulent components (figures 12 and 14), we found that the magnitudes of $-\overline{\tilde{u}\tilde{w}}/u_*^2$ are approximately one-quarter of those of $-\overline{u'w'}/u_*^2$ for

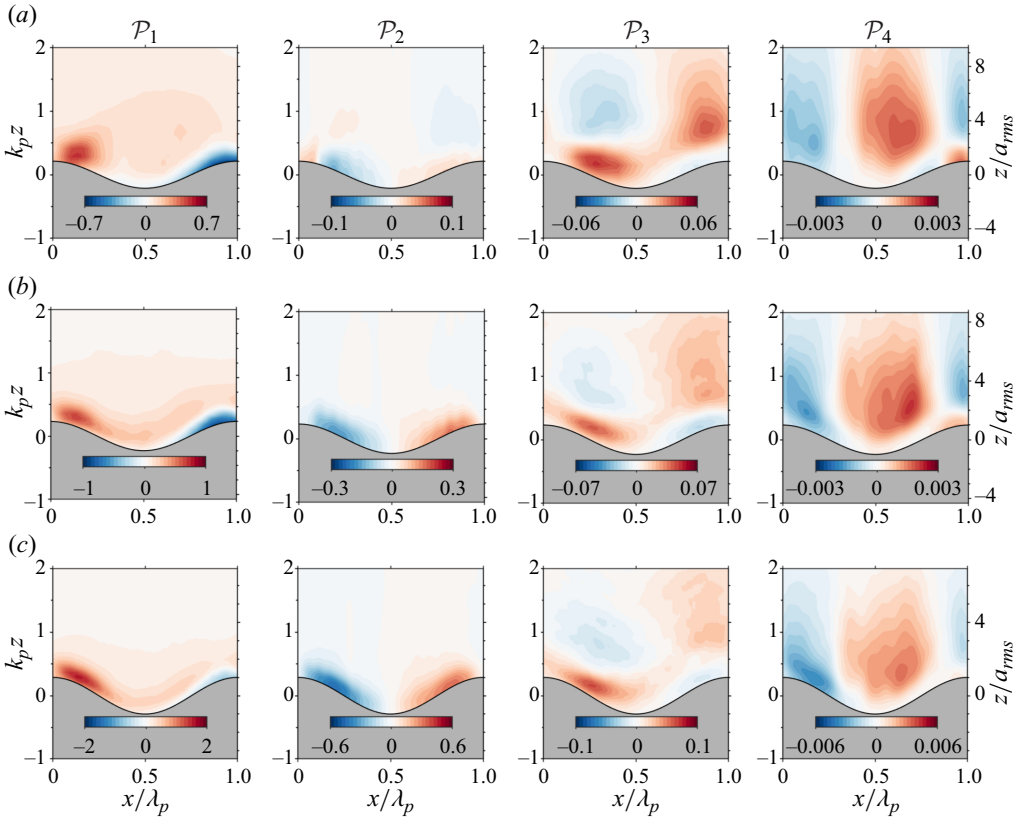

Figure 15. Phase-averaged shear production terms normalized by $100u_*^3/\lambda_p$ at: (*a*) $U_{ref} = 6.0$ m s^{-1}; (*b*) $U_{ref} = 8.0$ m s^{-1}; (*c*) $U_{ref} = 10.0$ m s^{-1}. Note that the wind blows from left to right and there is variation present on the contour colour bars from panel to panel.

the case of $U_{ref} = 6.0$ m s^{-1}, and the magnitude difference between $-\overline{\tilde{u}\tilde{w}}/u_*^2$ and $-\overline{u'w'}/u_*^2$ increases with increasing wind speed. This indicates a decreasing wave effect to air flow and the flow becomes more turbulent with increasing wind speed. The small wave-induced stresses compared with turbulent shear stresses are consistent with the results in the case of $U_{10} = 2.19$ m s^{-1} ($c_p/u_* = 6.5$) at a fetch of 22.7 m observed by Buckley & Veron (2019). We note that this case of Buckley & Veron (2019) is the only one that falls within the same wind-wave category III as those in our study, i.e. microscale breaking waves (figure 9). For the cases in different wind-wave categories, i.e. wave age of 2.5 and 1.4, similar magnitudes of wave-induced stresses and Reynolds stresses were found (Buckley & Veron 2019). These results suggest that wind-wave categories and stages can significantly affect the mechanism of wave influence on the turbulence and wave-induced flow above the water surface.

5. Turbulent kinetic energy budgets

The governing equation of the TKE budget for the air flow over wind waves under a steady-state condition can be written as (Reynolds & Hussain 1972; Calhoun & Street 2001)

$$\varepsilon = \mathcal{P} + \mathcal{A} + \mathcal{T}^t + \mathcal{T}^p + \mathcal{D}^v, \tag{5.1}$$

where $\mathcal{P}$ is the shear production; ε is the dissipation rate of TKE; $\mathcal{A}$ is the advection; $\mathcal{T}^t$ is the turbulence transport; $\mathcal{T}^p$ is the pressure transport and $\mathcal{D}^\nu$ is the viscous diffusion.

5.1. *Production term*

The production of TKE in the phase-averaged spatial domain consists of four terms (Calhoun & Street 2001; Yang & Shen 2010; Buckley & Veron 2019):

$$\mathcal{P} = \mathcal{P}_1 + \mathcal{P}_2 + \mathcal{P}_3 + \mathcal{P}_4, \tag{5.2}$$

$$\mathcal{P}_1 = -\langle u'w'\rangle \frac{\partial \langle u\rangle}{\partial z}, \quad \mathcal{P}_2 = -\langle u'^2\rangle \frac{\partial \langle u\rangle}{\partial x}, \quad \mathcal{P}_3 = -\langle w'^2\rangle \frac{\partial \langle w\rangle}{\partial z}, \quad \mathcal{P}_4 = -\langle u'w'\rangle \frac{\partial \langle w\rangle}{\partial x}. \tag{5.3a–d}$$

To illustrate the contribution of each term to the production of TKE, the phase-averaged $\mathcal{P}_1$, $\mathcal{P}_2$, $\mathcal{P}_3$ and $\mathcal{P}_4$ normalized by $100u_*^3/\lambda_p$, following Calhoun & Street (2001) and Yang & Shen (2010), are plotted in figure 15. Among the four terms, the shear production term $\mathcal{P}_1$ is the dominant term, which is generally one order of magnitude larger than $\mathcal{P}_2$ and $\mathcal{P}_3$, and two orders of magnitude larger than $\mathcal{P}_4$. Positive $\mathcal{P}_1$ is primarily concentrated on the leeward side, indicating that the majority of TKE production occurred in that region. A relatively small region of negative $\mathcal{P}_1$ is located near the water surface on the windward side. The negative shear production coincides with the negative Reynolds shear stress (figure 13), which may be attributed to the deceleration at that location when the wave travelling velocity is lower than the air flow for growing young waves. Here, $\mathcal{P}_2$ and $\mathcal{P}_3$ have similar patterns and show opposite signs in the spatial distribution. For instance, near the leeward side water surface, $\mathcal{P}_2$ is negative and $\mathcal{P}_3$ is positive, while $\mathcal{P}_2$ is positive but $\mathcal{P}_3$ is negative away from the surface. Although $\mathcal{P}_2$ and $\mathcal{P}_3$ are generally smaller than $\mathcal{P}_1$, accurate estimate of TKE production should include these terms. Especially close to the wavy surface, these two terms are not negligible. This is because the mean flow patterns are significantly altered near the wavy surface, which contributes to the production of turbulence that are associated with large gradients of velocities in addition to $\partial\langle u\rangle/\partial z$. Here, $\mathcal{P}_4$ is positive above the trough and negative above the crest. These general patterns of production terms are also similar to those over a stationary wavy surface (Calhoun & Street 2001) and wind generated waves with a longer fetch (Buckley & Veron 2019).

The relative importance of each component in the TKE production varies with wave ages. Within our narrow wave age range (1.03–1.10), $\mathcal{P}_1$ is the single dominant term. Yang & Shen (2010) reported that $\mathcal{P}_1$ is dominant with the wave age of 2, 14 and 25. Yang & Shen (2010) also noted that $\mathcal{P}_3$ and $\mathcal{P}_4$ are one order of magnitude smaller, different from what we observed: $\mathcal{P}_4$ is one order of magnitude smaller than $\mathcal{P}_3$ and $\mathcal{P}_2$, and two orders of magnitude smaller than $\mathcal{P}_1$. However, both Yang & Shen (2010) and our observation suggest the dominant role of $\mathcal{P}_1$ in turbulence production in slow, young waves as that in the solid wavy boundary layer. Buckley & Veron (2019) observed that $\mathcal{P}_1$ and $\mathcal{P}_2$ are one order of magnitude larger than $\mathcal{P}_3$ and $\mathcal{P}_4$ with wave age of 1.4, 2.5 and 6.5, equivalent to the wind speed of 16.63, 9.41 and 2.19 m s^{-1}, respectively. Their observation also shows that $\mathcal{P}_2$ was similar to $\mathcal{P}_1$, and gradually took over and became larger than $\mathcal{P}_1$ in their case with the highest wind speed and the youngest wave. This is different from our observation and the numerical simulation of Yang & Shen (2010). We note that the experiment of Buckley & Veron (2019) was conducted at a 22.7 m fetch, and their young waves are within the gravity wave regime where wave energy is primarily dissipated by micro- and macroscale breaking waves (figure 9). Air entrainment has likely occurred, which may have also altered the mechanism of turbulence production. In our observation,

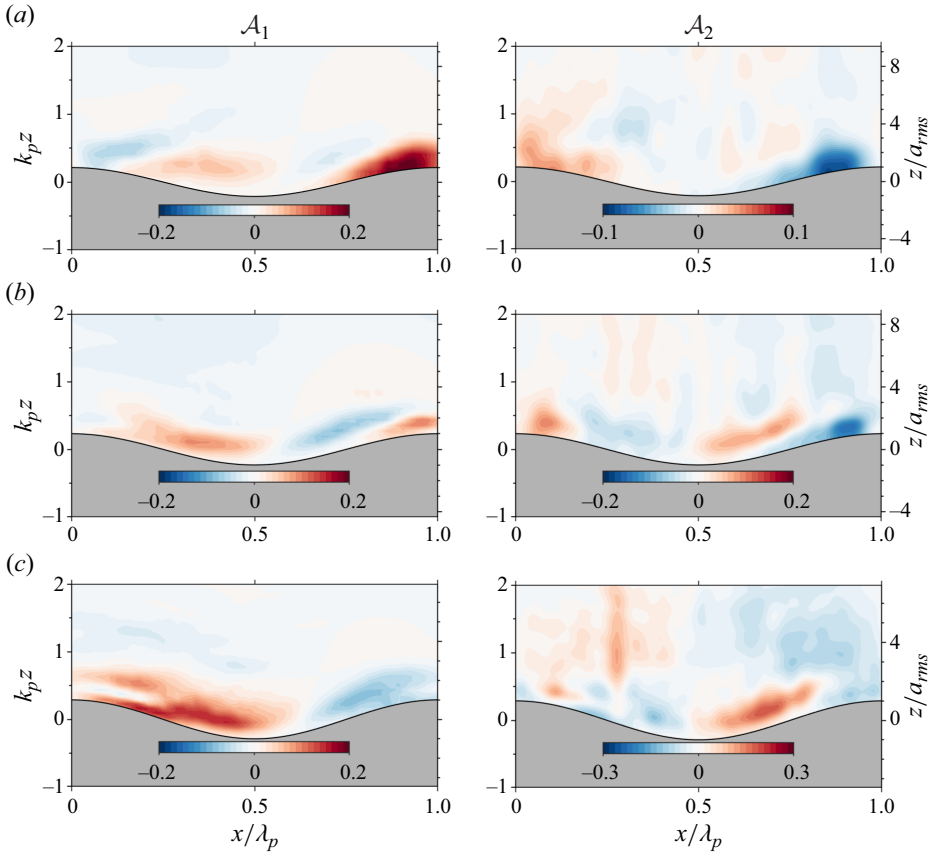

Figure 16. Phase-averaged advection terms normalized by $100u_*^3/\lambda_p$ at: (*a*) $U_{ref} = 6.0$ m s^{-1}; (*b*) $U_{ref} = 8.0$ m s^{-1}; (*c*) $U_{ref} = 10.0$ m s^{-1}. Note that the wind blows from left to right and there is variation present on the contour colour bars from panel to panel.

TKE production has a consistent mechanism across the wave category III: the Reynold shear stress works against the mean flow gradient, which transfers kinetic energy from the mean flow to the turbulence field.

5.2. *Advection term*

The phase-averaged advection of TKE by mean flow is defined as follows:

$$\mathcal{A} = \mathcal{A}_1 + \mathcal{A}_2, \quad \mathcal{A}_1 = -\langle w \rangle \frac{\partial \langle q \rangle}{\partial z} \quad \text{and} \quad \mathcal{A}_2 = -\langle u \rangle \frac{\partial \langle q \rangle}{\partial x}, \tag{5.4a–c}$$

where q is the TKE, taking a value of $(u'u' + v'v' + w'w')/2$ with $v'v' = (u'u' + w'w')/2$ (Yousefi *et al*. 2021). The data show similar magnitudes for the vertical advection $\mathcal{A}_1$ and the horizontal advection $\mathcal{A}_2$ (figure 16). Intensified $\mathcal{A}_1$ is located mainly close to the water surface, with positive value on the leeward side and negative on the windward side. For the lowest wind, an intensified positive $\mathcal{A}_1$ zone appears above the windward side of the crest. Intensified but weaker $\mathcal{A}_2$ is observed close the water surface with an opposite sign of $\mathcal{A}_1$. With increasing speed, we found an additional but weaker positive $\mathcal{A}_1$ zone immediately past the wave crest. This region coincides with the location of the vortical structure past

the crest or air separation shown in figure 2(*a*). The presence of air separation may produce substantial vertical advection near the separation. This observation is consistent with the experimental results in air flow over hills (Poggi *et al*. 2008).

Compared with the turbulence production, the advection term is quite small. In a solid wavy surface, Calhoun & Street (2001) found that advection is negative on the leeward side and positive on the windward side at a short distance above the wavy boundary. They suggest that the mean flow carries TKE-rich fluid away from the peak turbulence production region on the leeward side, resulting in negative advection there. The TKE-rich fluid is advected toward the windward, upslope boundary, resulting in positive advection on the windward side. However, in our wind-wave boundary, such organized TKE advection was not observed. The negative advection seems to only appear on the leeward side above a positive zone of $\mathcal{A}_1$ for the case of $U_{ref} = 6.0$ m s^{-1}. For the other two cases, this negative advection zone is too weak to appear in the distribution plot. In addition, $\mathcal{A}_2$ seems to offset a substantial portion of $\mathcal{A}_1$ so that the net advection is quite weak. The difference of advection pattern between our measurements and those for a solid wavy boundary may be attributed to the travelling of water surface.

5.3. *Turbulent transport term*

The phase-averaged turbulent transport of TKE is defined as follows:

$$\mathcal{T}^t = \mathcal{T}_1^t + \mathcal{T}_2^t, \quad \mathcal{T}_1^t = -\frac{\partial \langle qw' \rangle}{\partial z} \quad \text{and} \quad \mathcal{T}_2^t = -\frac{\partial \langle qu' \rangle}{\partial x}. \tag{5.5a,b}$$

The data show that for all wind speeds, $\mathcal{T}_1^{\mathrm{t}}$ is a dominant term in the turbulent transport of TKE (figure 17), indicating the dominant role of turbulent eddies that carry and exchange TKE in the vertical direction. Here, $\mathcal{T}_1^{\mathrm{t}}$ is positive in a narrow region immediately adjacent to the water surface on the windward side and negative above the positive region. The result suggests that the redistribution of TKE due to turbulent motions mainly occurred in these areas ($k_p z < \sim 0.7$). In a high wind condition ($U_{ref} = 10.0$ m s^{-1}), the positive region of $\mathcal{T}_1^{\mathrm{t}}$ close to the wavy surface shrinks and the negative region extends towards the wave crest.

5.4. *Dissipation term*

A high turbulent dissipation rate occurred near the water surface and decreased away from the surface (figure 18). The leeward side generally has higher TKE dissipation than the windward side. The high dissipation rate at the leeward side coincides with the strong turbulence shear production in that region but closer to the crest. With increasing wind speed, both windward- and leeward-side dissipation become similar. Immediately above the trough, the dissipation rate is smaller due to the shelter effect of the wave slope. This sheltered region near the trough was also observed using LES with a wave age of 1.4 (Husain *et al*. 2019).

To further investigate turbulence dissipation and compare with that in the solid wall boundary layer, figure 19 plots the averaged dissipation rate across the entire phases with the corresponding canonical LOW scaling, $\varepsilon_{LOW} = u_*^3/\kappa z$, where κ is the von Kármán constant, taken as 0.41. The data show that the dissipation rate in the wind wave field has a similar decaying profile away from the boundary as that from solid walls, but the value of dissipation rate in the wind-wave field are approximately 60–78 % smaller than that

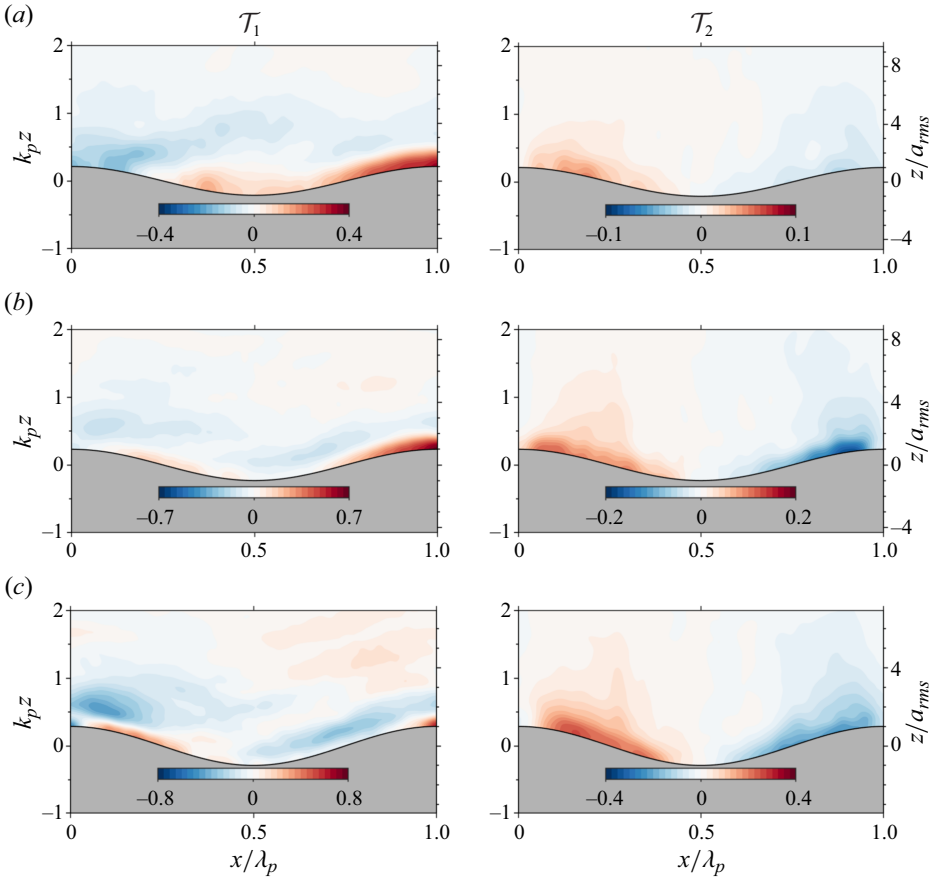

Figure 17. Phase-averaged turbulent transport terms normalized by $100u_*^3/\lambda_p$ at: (*a*) $U_{ref} = 6.0$ m s^{-1}; (*b*) $U_{ref} = 8.0$ m s^{-1}; (*c*) $U_{ref} = 10.0$ m s^{-1}. Note that the wind blows from left to right and there is variation present on the contour colour bars from panel to panel.

estimated using the LOW scaling. We found the mean ratio $\overline{\varepsilon/\varepsilon_{LOW}} = 0.21$, 0.35 and 0.40 for the cases of $U_{ref} = 6.0$, 8.0 and 10.0 m s^{-1}, respectively.

5.5. *Turbulent kinetic energy budget*

Finally, the phase-averaged TKE budget is illustrated in figure 20, which plots all budget terms and the residual term. In general, the three cases have similar spatial patterns of TKE budget terms, with subtle differences. All strong TKE budget terms are concentrated close to the water surface, except for the advection, which is patched in the entire measured region with weak substantial accumulations close to the surface.

To summarize, the mechanism of the TKE can be interpreted as follows: strong shear in the mean flow above the wave surface produces TKE close to the wave crest and extends downwind, leading to a high positive shear production region on the leeward side. Approaching the wave trough, shear production reduces substantially to zero and changes to negative values on the windward side near the surface. The spatial distribution of mean advection of TKE appears to be relatively weak with some intensification close to the surface. The relatively weak spatial distribution of TKE advection is due to the opposite

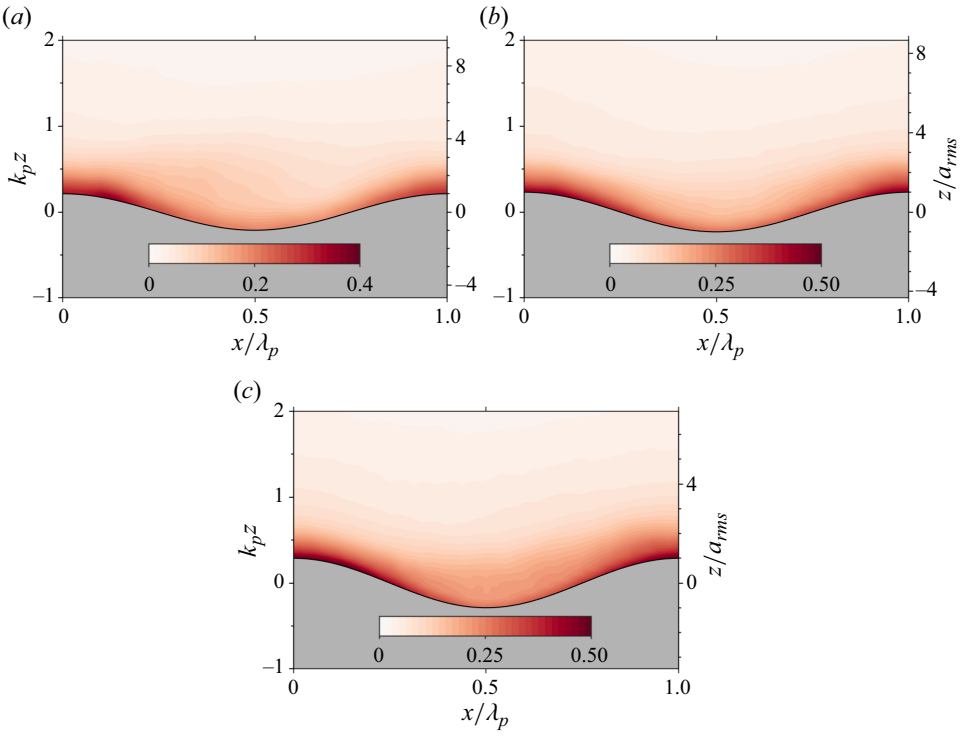

Figure 18. Phase-averaged turbulent dissipation ε normalized by $100u_*^3/\lambda_p$ at: (*a*) $U_{ref} = 6.0$ m s^{-1}; (*b*) $U_{ref} = 8.0$ m s^{-1}; (*c*) $U_{ref} = 10.0$ m s^{-1}. Note that the wind blows from left to right and there is variation present on the contour colour bars from panel to panel.

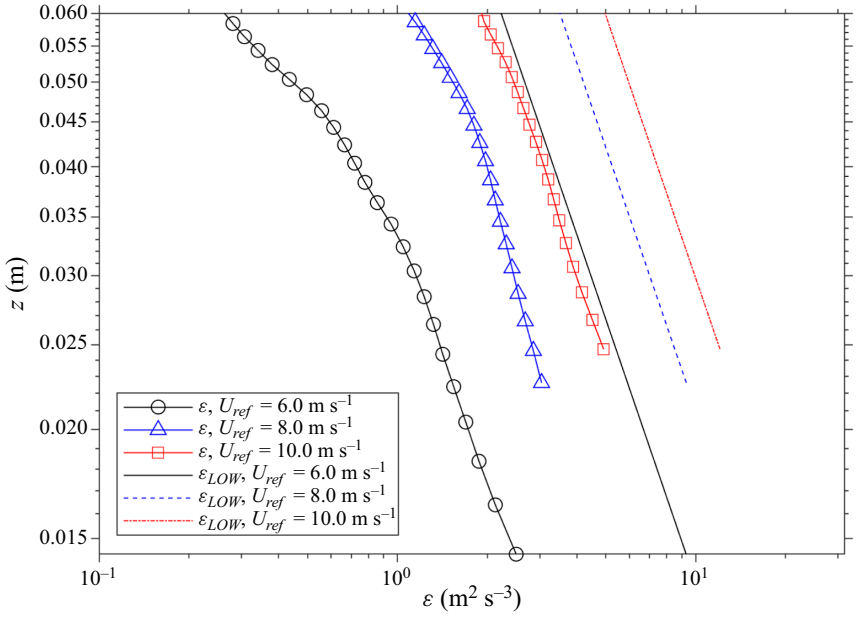

Figure 19. Vertical profile of turbulence dissipation rate: wind waves above water versus the corresponding law of the wall (LOW) above a solid boundary at the maximum wave height.

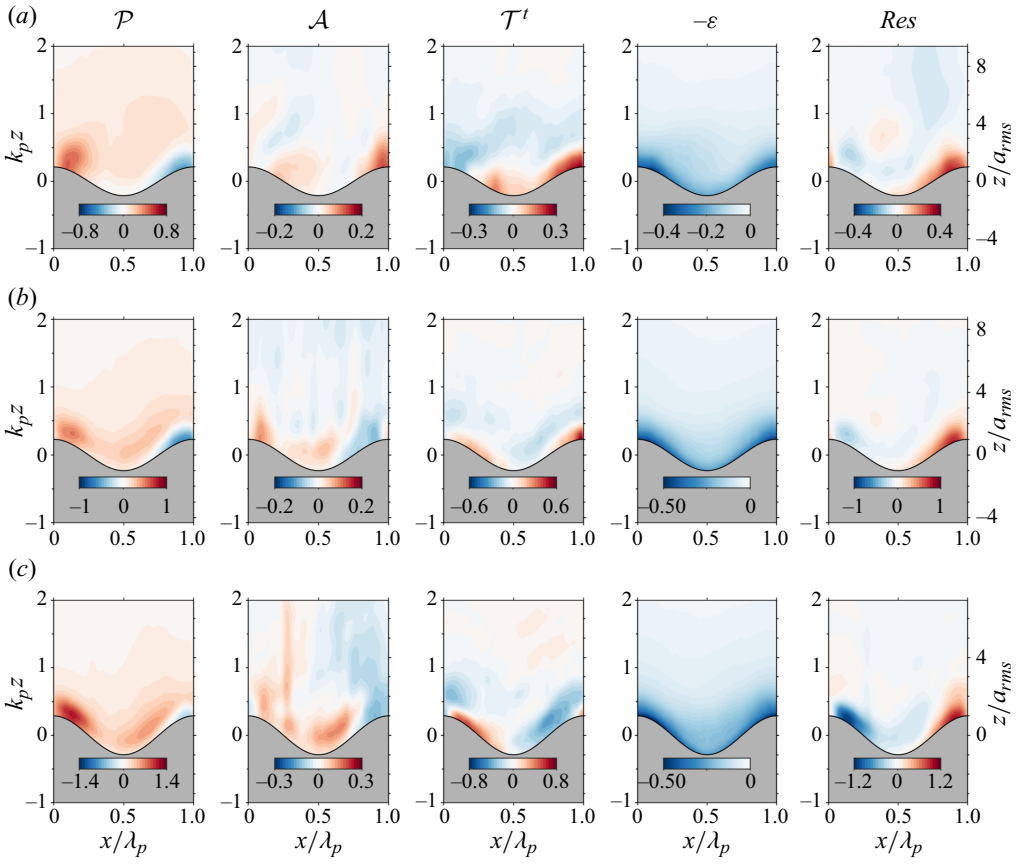

Figure 20. Phase-averaged shear production $\mathcal{P}$, advection $\mathcal{A}$, turbulent transport $\mathcal{T}^t$, turbulent dissipation ε and residual *Res* terms normalized by $100u_*^3/\lambda_p$ at: (*a*) $U_{ref} = 6.0$ m s^{-1}; (*b*) $U_{ref} = 8.0$ m s^{-1}; (*c*) $U_{ref} = 10.0$ m s^{-1}. Note that the wind blows from left to right and there is variation present on the contour colour bars from panel to panel.

effect of mean flow and TKE production. The mean velocity is small close to the water surface where most of the TKE is produced, whereas weaker TKE is produced in the high flow region away from the surface. The turbulent transport process redistributes the TKE through moving TKE-rich fluids to the low TKE region. Therefore, there is an accumulated negative turbulent transport region that coincides with the high TKE production region, which mainly moves the TKE towards the region close to the water surface, showing a thin layer of positive turbulent transport immediately above the water surface. Turbulent dissipation accumulated close to the surface primarily dissipates the TKE generated from the shear production, i.e. local equilibrium.

Taken together, we found that the residual term is substantial within one wave height and shows a distinct spatial distribution. Specifically, most residuals show the opposite sign of the production term for balancing the TKE budget. The viscous diffusion was calculated and found to be negligible in this study. Although the current calculation does not include the TKE transport caused by pressure, its contribution to the TKE budget is usually small (Yang & Shen 2010). Therefore, we suspect that the residual term is unlikely the result of an unresolved pressure transport term.

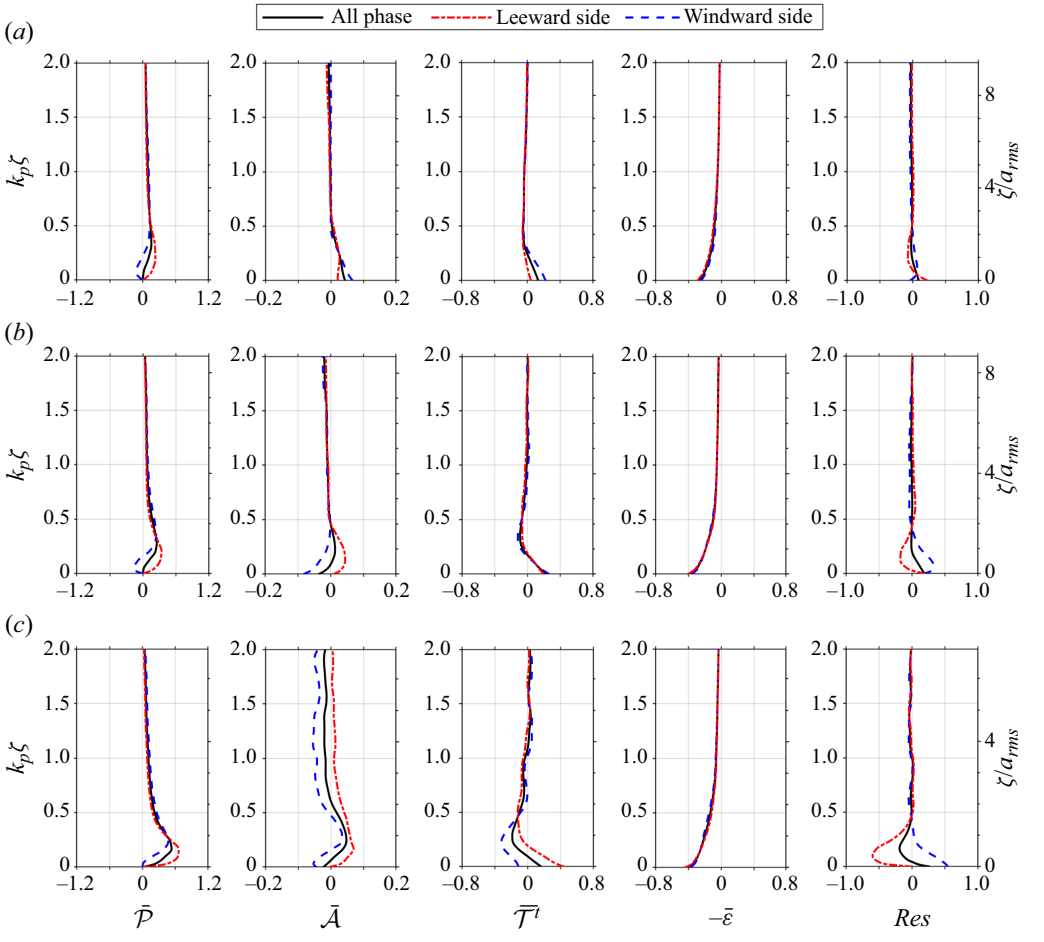

Figure 21. Averaged vertical profiles of turbulent kinetic energy budgets with averaging over all phase, leeward and windward sides: shear production $\bar{\mathcal{P}}$, advection $\bar{\mathcal{A}}$, turbulent transport $\overline{\mathcal{T}^t}$, turbulent dissipation $\bar{\varepsilon}$ and residual *Res* normalized by $100u_*^3/\lambda_p$ at: (*a*) $U_{ref} = 6.0$ m s^{-1}; (*b*) $U_{ref} = 8.0$ m s^{-1}; (*c*) $U_{ref} = 10.0$ m s^{-1}.

The difference in several TKE budget terms between windward and leeward sides of wind waves motivates us to examine them by conditional averaging based on the directions relative to the wind (figure 21). Not surprisingly, most differences occur within approximately one wave height ($\zeta < \sim 2a_{rms}$) above the water surface, except for the advection term (especially for the case of $U_{ref} = 10.0$ m s^{-1}). Consistently with the spatial distribution plot, turbulence production is larger on the leeward side, with the maximal value approximately twice that on the windward side. The peak production occurs between 0.5 and 1.5 wave amplitudes. Advection is relatively small, but the profiles of advection are not strictly consistent among all three cases. The turbulent transport is quite consistent on both sides. The negative turbulent transport term around the location of peak turbulence production indicates the mechanism of the turbulent transport, i.e. redistributing TKE from a TKE-rich to TKE-weak region. There seems to be no difference in TKE dissipation rate on leeward and windward sides. Together, the TKE is largely balanced for the three cases. Within one wave height, the residual appears to be positive on the windward side and negative on the leeward side, indicating that the TKE budget is not locally balanced at

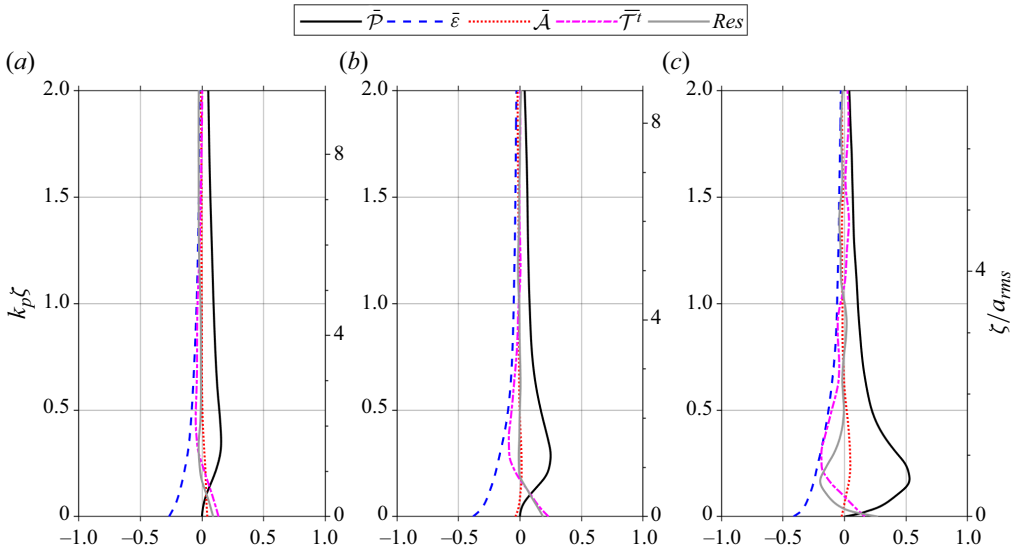

Figure 22. Averaged vertical profiles of turbulent kinetic energy budgets normalized by $100u_*^3/\lambda_p$ at: (*a*) $U_{ref} = 6.0$ m s^{-1}; (*b*) $U_{ref} = 8.0$ m s^{-1}; (*c*) $U_{ref} = 10.0$ m s^{-1}.

various phases. The difference of residual on windward and leeward sides substantially increases with increasing wind speed.

5.6. *Vertical profiles of averaged turbulent kinetic energy budgets*

The profiles of TKE budget terms averaged over all wave phases are plotted in figure 22. As discussed above, turbulence production occurs significantly close to the surface, with the peak at approximately $\zeta = 0.5a_{rms}$ to $\zeta = 1.5a_{rms}$. The advection is relatively small. Turbulent transport is a source immediately above the water surface and changes to a sink within $k_p\zeta = 0.1$–0.2. The turbulent dissipation rate is the primary sink term. The data indicate that the TKE budget is generally closed among these terms with relatively small residual for the two low wind conditions. There is a noticeable negative residual within $\zeta < a_{rms}$ for the highest wind speed condition. The peak magnitude of the residual is approximately half of the peak shear production. While the measurement uncertainty in high-order turbulence terms very close to the water surface may be a contributor, the exact cause of the observed residual is subject to future explorations.

Although the TKE budgets seem balanced, the production-dissipation ratio $\bar{\mathcal{P}}/\bar{\varepsilon}$ is 1.49, 1.48 and 2.18 at $\zeta = 1.6a_{rms}$, $1.2a_{rms}$ and $0.6a_{rms}$ for the case of $U_{ref} = 6.0$, 8.0 and 10.0 m s^{-1}, respectively, based on the location where the production is at a peak. The results for the two lower wind cases are slightly smaller than the production-dissipation ratio of 1.6 from numerical simulation with a wave age of 2 (Yang & Shen 2010). The ratios are much smaller than the production-dissipation ratio of 3 reported by Shaikh & Siddiqui (2010) with a wave age of approximately 2. The difference may be due to the method used for calculating the dissipation rate. For instance, our calculation indicates that the 'direct method' based on coarse-resolution PIV measurements without calibration may substantially underestimate the turbulence dissipation rate. With our data, we found that the production-dissipation ratio for the case of $U_{ref} = 10.0$ m s^{-1} is approximately 45 % higher than the other two cases. We note that this case lies on the

boundary of wave regimes III–IV, where substantial increase of microscale breaking waves would occur (Siddiqui & Loewen, 2007). Therefore, we suspect that the increase in the production-dissipation ratio may be attributed to the increased surface roughness due to the onset (or near onset) of macroscale breakers and the significant coverage of microscale breakers on the water surface (figure 8).

6. Conclusions

In this paper, we presented an experimental study using particle image velocimetry (PIV) to resolve the turbulence structure over the wind waves and to analyse the budget of turbulent kinetic energy (TKE) of the overlying airflow. The experiment was designed to focus on developing young waves (i.e. $c_p/u_* = 1.03$–1.10) with a short fetch (i.e. $F = 6.2$ m), which were travelling slower than the bulk air flow velocity (i.e. wind-driven sea).

Using measured wave characteristics and the data from the literature, we found a dimensionless power-law relationship between Bond number and Reynolds number based on shear velocity and fetch: $Bo \sim Re_*^{8/5}$, which can be used to classify the wave regime depending on the primary mechanism of the wave energy dissipation. Although all wind waves are young in this study, they represent the entire regime of the wave category III, where the wave energy is mainly dissipated by capillaries and microscale breakers. The case of $U_{ref} = 6.0$ m s^{-1} is close to the wave category II, and hence represents the early stage of wave category III, i.e. the water surface was primarily covered by capillaries with onset of microscale breaking. The case of $U_{ref} = 10.0$ m s^{-1} is close to the wave category IV, and hence represents the late stage of wave category III, where the water surface was primarily covered by microscale breakers with onset of macro-breaking.

Through velocity triple-decomposition, our analysis provided the structures of wave-induced flow and the phase-independent turbulent flow above the varying phases of the waves. Our result demonstrated that the turbulent intensities and the velocity fluctuation-induced stresses are at least four times larger than the wave-induced counterparts, indicating that weaker kinetic energy in the air flow is coherent with wave motions and stronger kinetic energy is associated with phase-independent turbulence. However, the turbulent intensities were suppressed close to the wave boundary, where the organized turbulent motions generated intensified turbulent Reynolds shear stress on the leeward side of the waves.

The structures of TKE budget terms illustrate the wave-related spatial distributions of production, advection, transport and dissipation of the TKE. In a young wave covered by microscale breakers, the shear production dominated the generation of TKE, where the contributions from the normal stresses were small. This TKE generation mechanism is similar to that for solid wavy boundaries, and differs from those for the old waves or young waves at strong wind and long fetches that might be covered by macroscale breakers. In addition, the leeward side turbulence production was approximately twice of that on the windward side. The advection was weak compared with the TKE production. The turbulent transport term acted as expected, transporting the TKE away from the high turbulence production region.

Time-resolved PIV allowed us to estimate the dissipation rate of TKE above the wavy surface using the spectral fitting method to calibrate the directly calculated values from velocity gradients. Using an adequate sampling frequency, we resolved the universal Kolmogorov scaling in the inertial subrange of the energy cascade, which was used to estimate the turbulent dissipation rate that was not biased by the coarse spatial resolution

in the PIV measurement. The data show that the intensified turbulent dissipation rate occurred at the wave crest, which coincided with the strong shear production in that region. The region immediately above the wave trough was sheltered by the leeward wave slope and showed weaker turbulence dissipation. The turbulent dissipation rates above the wind waves in our study were approximately 60–78 % smaller than those following the canonical law-of-the-wall (LOW) scaling.

Finally, the TKE budget analysis showed that the turbulence production, advection, turbulent transport and dissipation were generally in balance in all three cases. Although the TKE budgets seem balanced, the production-dissipation ratio for the highest wind speed was increased by 45 % compared with that for the two lower wind speeds. The increase of production-dissipation ratio might be caused by the increased roughness over the significant coverage of micro-breaking waves and near onset of macro-breakers. Further studies are needed to clarify this phenomenon.

Declaration of interests. The authors report no conflict of interest.

Author ORCIDs.
Binbin Wang https://orcid.org/0000-0003-3799-2042;
Kuang-An Chang https://orcid.org/0000-0003-3177-4896.

References

Banner, M.L. & Phillips, O.M. 1974 On the incipient breaking of small scale waves. *J. Fluid Mech.* **65** (4), 647–656.

Blennerhassett, P.J. & Stuart, J.T. 1997 On the generation of waves by wind. *Phil. Trans. R. Soc. Lond.* A, *Math. Phys. Sci.* **298** (1441), 451–494.

Buckley, M.P. & Veron, F. 2016 Structure of the airflow above surface waves. *J. Phys. Oceanogr.* **46** (5), 1377–1397.

Buckley, M.P. & Veron, F. 2019 The turbulent airflow over wind generated surface waves. *Eur. J. Mech.* B-*Fluids* **73**, 132–143.

Calhoun, R.J. & Street, R.L. 2001 Turbulent flow over a wavy surface: neutral case. *J. Geophys. Res.: Oceans* **106** (C5), 9277–9293.

Caulliez, G. 2013 Dissipation regimes for short wind waves. *J. Geophys. Res.: Oceans* **118** (2), 672–684.

Cox, C.S. 1958 Measurements of slopes of high-frequency wind waves. *J. Mar. Res.* **16**, 199–225.

Deike, L., Popinet, S. & Melville, W.K. 2015 Capillary effects on wave breaking. *J. Fluid Mech.* **769**, 541–569.

Doron, P., Bertuccioli, L., Katz, J. & Osborn, T. 2001 Turbulence characteristics and dissipation estimates in the coastal ocean bottom boundary layer from PIV data. *J. Phys. Oceanogr.* **31** (8), 2108–2134.

Duncan, J.H., Qiao, H., Philomin, V. & Wenz, A. 1999 Gentle spilling breakers: crest profile evolution. *J. Fluid Mech.* **379**, 191–222.

Hidy, G.M. & Plate, E.J. 1966 Wind action on water standing in a laboratory channel. *J. Fluid Mech.* **26** (4), 651–687.

Hsu, C.-T. & Hsu, E.Y. 1983 On the structure of turbulent flow over a progressive water wave: theory and experiment in a transformed wave-following coordinate system. Part 2. *J. Fluid Mech.* **131**, 123–153.

Hsu, C.-T., Hsu, E.Y. & Street, R.L. 1981 On the structure of turbulent flow over a progressive water wave: theory and experiment in a transformed, wave-following co-ordinate system. *J. Fluid Mech.* **105**, 87–117.

Hsu, C.-T., Wu, H.-Y., Hsu, E.-Y. & Street, R.L. 1982 Momentum and energy transfer in wind generation of waves. *J. Phys. Oceanogr.* **12** (9), 929–951.

Hudson, J.D., Dykhno, L. & Hanratty, T.J. 1996 Turbulence production in flow over a wavy wall. *Exp. Fluids* **20** (4), 257–265.

Husain, N.T., Hara, T., Buckley, M.P., Yousefi, K., Veron, F. & Sullivan, P.P. 2019 Boundary layer turbulence over surface waves in a strongly forced condition: LES and observation. *J. Phys. Oceanogr.* **49** (8), 1997–2015.

Jessup, A.T., Zappa, C.J. & Yeh, H. 1997 Defining and quantifying microscale wave breaking with infrared imagery. *J. Geophys. Res.: Oceans* **102** (C10), 23145–23153.

JOHNSON, B.A. & COWEN, E.A. 2018 Turbulent boundary layers absent mean shear. *J. Fluid Mech.* **835**, 217–251.

KEANE, R.D. & ADRIAN, R.J. 1992 Theory of cross-correlation analysis of PIV images. *Appl. Sci. Res.* **49** (3), 191–215.

KOLMOGOROV, A.N. 1941 The local structure of turbulence in incompressible viscous fluid for very large Reynolds number. *Dokl. Akad. Nauk. SSSR* **30**, 301–303.

KOMEN, G.J. 1980 Nonlinear contributions to the frequency spectrum of wind-generated water waves. *J. Phys. Oceanogr.* **10** (5), 779–790.

LAKE, B.M. & YUEN, H.C. 1978 A new model for nonlinear wind waves. Part 1. Physical model and experimental evidence. *J. Fluid Mech.* **88** (1), 33–62.

LAMONT-SMITH, T. & WASEDA, T. 2008 Wind wave growth at short fetch. *J. Phys. Oceanogr.* **38** (7), 1597–1606.

LI, G., ELLIOTT, C.M., CALL, B.C., SANSOM, B.J., JACOBSON, R.B. & WANG, B. 2023 Turbulence near a sandbar island in the lower Missouri River. *River Res. Appl.* **39** (9), 1857–1874.

LOEWEN, M.R. & SIDDIQUI, M.H.K. 2006 Detecting microscale breaking waves. *Meas. Sci. Technol.* **17** (4), 771.

LUZNIK, L., ZHU, W., GURKA, R., KATZ, J., SMITH, W.A.M.N. & OSBORN, T.R. 2007 Distribution of energy spectra, Reynolds stresses, turbulence production, and dissipation in a tidally driven bottom boundary layer. *J. Phys. Oceanogr.* **37** (6), 1527–1550.

MELVILLE, W.K. 1983 Wave modulation and breakdown. *J. Fluid Mech.* **128**, 489–506.

MILES, J.W. 1957 On the generation of surface waves by shear flows. *J. Fluid Mech.* **3** (2), 185–204.

ORTIZ-SUSLOW, D.G. & WANG, Q. 2019 An evaluation of Kolmogorov's −5/3 power law observed within the turbulent airflow above the ocean. *Geophys. Res. Lett.* **46** (24), 14901–14911.

ORTIZ-SUSLOW, D.G., WANG, Q., KALOGIROS, J. & YAMAGUCHI, R. 2020 A method for identifying Kolmogorov's inertial subrange in the velocity variance spectrum. *J. Atmos. Ocean. Technol.* **37** (1), 85–102.

PHILLIPS, O.M. 1957 On the generation of waves by turbulent wind. *J. Fluid Mech.* **2** (5), 417–445.

PIZZO, N., DEIKE, L. & AYET, A. 2021 How does the wind generate waves? *Phys. Today* **74** (11), 38–43.

POGGI, D., KATUL, G.G., FINNIGAN, J.J. & BELCHER, S.E. 2008 Analytical models for the mean flow inside dense canopies on gentle hilly terrain. *Q. J. R. Meteorol. Soc.* **134** (634), 1095–1112.

PORCHETTA, S., CARLESI, T., VETRANO, M.R., VAN BEECK, J. & LABOUREUR, D. 2022 Experimental investigation of the airflow structure above mechanically generated regular waves for both aligned and opposed wind–wave directions. *Exp. Therm. Fluid Sci.* **133**, 110578.

RAFFEL, M., WILLERT, C.E., & KOMPENHANS, J. 1998 *Particle Image Velocimetry: A Practical Guide*, vol. 2. Springer.

REUL, N., BRANGER, H. & GIOVANANGELI, J.-P. 1999 Air flow separation over unsteady breaking waves. *Phys. Fluids* **11** (7), 1959–1961.

REUL, N., BRANGER, H. & GIOVANANGELI, J.-P. 2008 Air flow structure over short-gravity breaking water waves. *Boundary-Layer Meteorol.* **126** (3), 477–505.

REYNOLDS, W.C. & HUSSAIN, A.K.M.F. 1972 The mechanics of an organized wave in turbulent shear flow. Part 3. Theoretical models and comparisons with experiments. *J. Fluid Mech.* **54** (2), 263–288.

RUTGERSSON, A. & SULLIVAN, P.P. 2005 The effect of idealized water waves on the turbulence structure and kinetic energy budgets in the overlying airflow. *Dyn. Atmos. Oceans* **38** (3), 147–171.

SAARENRINNE, P. & PIIRTO, M. 2000 Turbulent kinetic energy dissipation rate estimation from PIV velocity vector fields. *Exp. Fluids* **29** (1), S300–S307.

SHAIKH, N. & SIDDIQUI, K. 2010 An experimental investigation of the near surface flow over air-water and air-solid interfaces. *Phys. Fluids* **22** (2), 025103.

SHEN, L., ZHANG, X., YUE, D.K.P. & TRIANTAFYLLOU, M.S. 2003 Turbulent flow over a flexible wall undergoing a streamwise travelling wave motion. *J. Fluid Mech.* **484**, 197–221.

SIDDIQUI, M.H.K. & LOEWEN, M.R. 2007 Characteristics of the wind drift layer and microscale breaking waves. *J. Fluid Mech.* **573**, 417–456.

STEWART, R.H. 1970 Laboratory studies of the velocity field over deep-water waves. *J. Fluid Mech.* **42** (4), 733–754.

SULLIVAN, P.P. & MCWILLIAMS, J.C. 2010 Dynamics of winds and currents coupled to surface waves. *Annu. Rev. Fluid Mech.* **50** (42), 19–42.

SULLIVAN, P.P., MCWILLIAMS, J.C. & MOENG, C.-H. 2000 Simulation of turbulent flow over idealized water waves. *J. Fluid Mech.* **404**, 47–85.

TENNEKES, H. & LUMLEY, J.L. 1972 *A First Course in Turbulence*. MIT.

TOBA, Y. 1961 Drop production by bursting of air-bubbles on the sea surface III. Study by use of wind flume. *Mem. Coll. Sci. Univ. Kyoto Ser.* A **3**, 313–344.

TOBA, Y. 1972 Local balance in the air-sea boundary processes. *J. Oceanogr.* **28** (3), 109–120.

WANG, B. & LIAO, Q. 2016 Field observations of turbulent dissipation rate profiles immediately below the air-water interface. *J. Geophys. Res. Oceans* **121** (6), 4377–4391.

WANG, B., LIAO, Q., FILLINGHAM, J.H. & BOOTSMA, H.A. 2015 On the coefficients of small eddy and surface divergence models for the air-water gas transfer velocity. *J. Geophys. Res. Oceans* **120** (3), 2129–2146.

WU, H., WANG, B., DIMARCO, S.F. & TAN, L. 2021 Impact of bubble size on turbulent statistics in bubble plumes in unstratified quiescent water. *Intl J. Multiphase Flow* **141**, 103692.

WU, J. 1971 Anemometer height in Froude scaling of wind stress. *J. Waterways Harbors Coastl Engng Div.* **97** (1), 131–137.

WU, J. 1973 Prediction of near-surface drift currents from wind velocity. *J. Hydraul. Div.* **99** (9), 1291–1302.

WU, J. 1975 Wind-induced drift currents. *J. Fluid Mech.* **68** (1), 49–70.

WU, J. & DEIKE, L. 2021 Wind wave growth in the viscous regime. *Phys. Rev. Fluids* **6** (9), 094801.

XU, D. & CHEN, J. 2013 Accurate estimate of turbulent dissipation rate using PIV data. *Exp. Therm. Fluid Sci.* **44**, 662–672.

YANG, D. & SHEN, L. 2010 Direct-simulation-based study of turbulent flow over various waving boundaries. *J. Fluid Mech.* **650**, 131–180.

YOUSEFI, K. & VERON, F. 2020 Boundary layer formulations in orthogonal curvilinear coordinates for flow over wind-generated surface waves. *J. Fluid Mech.* **888**, A11.

YOUSEFI, K., VERON, F. & BUCKLEY, M.P. 2021 Turbulent and wave kinetic energy budgets in the airflow over wind-generated surface waves. *J. Fluid Mech.* **920**, A33.

ZAPPA, C.J., ASHER, W.E., JESSUP, A.T., KLINKE, J. & LONG, S.R. 2004 Microbreaking and the enhancement of air-water transfer velocity. *J. Geophys. Res. Oceans* **109**, C8.

ZHANG, X. 1995 Capillary–gravity and capillary waves generated in a wind wave tank: observations and theories. *J. Fluid Mech.* **289**, 51–82.